Quaternary International 732 (2025) 109804

Contents lists available at ScienceDirect

Quaternary International

journal homepage: www.elsevier.com/locate/quaint

Earthquake environmental effects and ESI 2007 of the 6th February 2023 Kahramanmaraş earthquakes along the East Anatolian Fault Zone (Türkiye)

Sarah J. Boulton [a,*], Joshua N. Jones [b], Fatma S. Malcioglu [c], Aisling O'Kane [d,e], Matthew D. Cleave [a], Orestis Adamidis [f], Teoman Efeoglu [g], Yasemin Didem Aktaş [h]

[a] School of Geography, Earth and Environmental Sciences, University of Plymouth, Plymouth, PL4 8AA, UK
[b] AECOM Ltd, East Wing Plumer House, Plymouth, UK
[c] Department of Earthquake Engineering, Kandilli Observatory and Earthquake Research Institute, Boğaziçi University, İstanbul, Türkiye
[d] Department of Geohazards and Tectonics, School of Earth and Environment, University of Canterbury, Christchurch, New Zealand
[e] GNS Science, Avalon Site, Lower Hutt, New Zealand
[f] Department of Engineering Science, University of Oxford, Oxford, OX1 3PJ, UK
[g] Department of Civil Engineering, University of Bristol, Bristol, UK
[h] Department of Civil, Environmental and Geomatic Engineering, University College London (UCL), London, UK

ARTICLE INFO

Keywords:
Kahramanmaraş earthquakes
Türkiye
Syria
Earthquake environmental effects (EEEs)
ESI-2007
EEFIT

ABSTRACT

The February 6, 2023 Kahramanmaraş earthquake doublet resulted in a range of devasting impacts on the built and natural environments. Here the macroseimic intensity of the event is assessed using the Environmental Seismic Intensity Scale (ESI 2007), which considers a range of primary and secondary earthquake environmental effects (EEEs) resulting from the causative earthquakes. These features were documented as part of the hybrid Earthquake Engineering Field Investigation Team (EEFIT) mission and by numerous other studies in the aftermath of the earthquakes. The primary fault ruptures along segments of the East Anatolian Fault Zone exceeded 350 km along the Pazarcık segment (the first fault to rupture) with a maximum displacement (D_{max}) of ~8 m, and 150 km with a D_{max} ~7–8 m along the Çardak-Sürgü Fault, which subsequently ruptured later the same day in an event termed the Elbistan or Ekinözü earthquake. In addition, a range of other secondary effects such as landslides and rockfalls, liquefaction and lateral spreading, changes to springs, tsunami and widespread damage were reported over an area >35,000 km^2. These data indicate epicentral intensities of XI and X for the Pazarcık and Elbistan earthquakes, respectively, consistent with the intensity inferred from measured offsets along these faults. Whereas site intensities based upon various secondary effects range from VIII – XI. Given the close association in time and space of the two main shock events it is difficult to attribute the wider off-fault secondary features to either event, especially where the faults converge in the north, but there is good correlation with: a) the mapped fault traces and many documented EEEs occur with 10–15 km of the rupture; and b) measured peak ground acceleration (PGA), where ESI 2007 intensities of > X correspond to regions experiencing >0.2 g PGA, and there are a few EEEs where PGA did not exceed 0.05 g. However, both maximum reported moment magnitude intensity (MMI) and Did You Feel It (DYFI) reports are 1–3° lower than the ESI 2007 values derived here, possibly resulting from bias towards urban areas. These data not only highlight the utility of using environmental effects in earthquake intensity studies but also suggest that the Kahramanmaraş earthquakes are unprecedented within the historical record of the region.

1. Introduction

On the February 6, 2023, at 01:17 UTC, a Mw 7.8 earthquake occurred along the East Anatolian Fault Zone (EAFZ) of south-central Türkiye (generally termed the Pazarcık earthquake). Later that day, at 10:24 UTC, another Mw 7.5 earthquake ruptured the Çardak – Sürgü Fault to the NW (variously called the Elbistan or Ekinözü earthquake). These earthquakes, collectively called the Kahramanmaraş earthquakes, resulted in an estimated $84 billion dollars of damage in Türkiye alone and sadly the loss of >65,000 lives across Syria and Türkiye.

* Corresponding author.
E-mail address: sarah.boulton@plymouth.ac.uk (S.J. Boulton).

https://doi.org/10.1016/j.quaint.2025.109804
Received 2 January 2025; Received in revised form 26 March 2025; Accepted 17 April 2025
Available online 27 April 2025

In addition, to the severe damage seen in the built environment, these events caused widespread environmental effects. Earthquake Environmental Effects (EEEs) refer to a number of changes to the natural environment as a result of a seismic event and can be defined as either primary or secondary effects. Primary effects are the direct surface expression of the earthquake (i.e., surface ruptures or faulting, tectonic subsidence or uplift), while secondary effects are caused by the wider ground shaking (i.e., landslides, liquefaction, ground water changes etc.).

While EEEs have long been recognised from the earliest studies of co-seismic deformation (e.g., Cornish, 1908), and were included in early seismic intensity scales (i.e., Davison, 1921), more recent intensity scales omitted environmental factors to focus on the built environment. The recognition that key environmental information was being overlooked in these more recent scales led to the development of the Environment Seismic Intensity 2007 Scale (ESI 2007; Michetti et al., 2004, 2007; Silva et al., 2015) under the auspices of INQUA (International Union for Quaternary Research). This twelve-point intensity scale considers both primary and secondary effects to provide a quantitative analysis of the EEEs and can be used independently or along-side other intensity scales. The ESI 2007 scale has advantages in that it can be compared to, or applied to, historic and palaeo-seismic events (i.e., Reicherter et al., 2009), used in areas of sparse or no population (i.e., Mosquera-Machado et al., 2009), and in different socio-economic or cultural regions, where building damage may reflect local building typologies rather than earthquake properties (Serva, 1994; Michetti et al., 2007). Consequently the ESI 2007 scale has been applied to numerous recent and historical events globally (Ferrario et al., 2022), including earthquakes in Greece (Papanikolaou and Melaki, 2017), Columbia (Mosquera-Machado et al., 2009), Japan and Taiwan (Ota et al., 2009; Naik et al., 2023) and is now regarded as a key tool in seismic hazard assessment (Ferrario et al., 2022; Papanikolaou et al., 2015; Reicherter et al., 2009). However, there is still a need to add to these existing assessments to test empirical relationships with large magnitude events and strike-slip earthquakes, which are relatively under-represented compared to reverse and normal faults events in the database of earthquakes with documented ESI 2007 intensities (Ferrario et al., 2022).

This paper presents a synthesis of EEE observations from the hybrid Earthquake Engineering Field Investigation Team (EEFIT) mission along with published reports to summarise the environmental effects induced by the 2023 Kahramanmaraş earthquakes that struck southern Türkiye and northern Syria. We then apply the ESI 2007 scale to these observations. Earthquake environmental effects are then compared to ground deformation measurements – Peak Ground Acceleration (PGA) and measurements of earthquake size in particular moment magnitude intensity, allowing a comparison to key historical events. This analysis highlights the unprecedented nature of these events and the need for future research in the region.

2. Geological and seismological background

2.1. Tectonic framework of the Eastern Mediterranean

The Eastern Mediterranean region is a classic example of ‘escape’ or ‘extrusion’ tectonics (c.f., Tapponnier et al., 1982) caused by the on-going contraction of the Mediterranean Sea as a result of the northward motion of the Arabian and African plates relative to a stable Eurasia. Continental collision in the region is likely to have begun in the Late Cretaceous with final closure of the Southern Neotethys, resulting in the formation of the Mediterranean Sea, thought to have occurred in the Oligocene (Allen and Armstrong, 2008; Robertson and Parlak, 2024). Continental collision was initially accommodated by crustal thickening and rapid uplift of the Anatolian Plateau (Şengör et al., 2008), which changed to extrusion in late Miocene to early Pleistocene time (Bozkurt, 2001; Şengör et al., 1985). The extrusion of the Anatolian microplate is accommodated along the North Anatolian and East Anatolian fault zones (Fig. 1) that take-up the westwards motion of Anatolia, driven in part by the northwards motion of Arabia but also by the roll-back of the Aegean subduction zone pulling the micro-plate to the west.

To the south of Anatolia, the relative motion between the African and Arabian plates is accommodated along the sinistral Dead Sea Fault Zone (DSFZ) (Fig. 1). The DSFZ links the area of sea-floor spreading in the Red Sea to the northern boundary of the Arabian plate and the zone of continental collision. The DSFZ initiated in the Miocene, around 20–18 Ma (Ben-Avraham, 1978; Lyberis et al., 1992; Weinberger et al., 2020) in the south and propagated northwards reaching southern Türkiye in the Late Miocene/Pliocene (Karabacak et al., 2010).

The East Anatolian Fault Zone (EAFZ) is also a sinistral strike-slip fault zone trending ~ NE-SW for >400 km from Karlıova in the east to the Mediterranean Sea. The fault likely initiated in the Late Pliocene (3–4 Ma; Saroglu, 1992; Westaway and Arger, 2001) and has an average long-term slip rate of 7–9 mm/yr (e.g., Reilinger et al., 2006). In the northeast the fault is mainly characterised by a single fault strand split into several segments (Fig. 1), defined by the changes in the strike of the fault, step-overs or pull-apart basins. However, towards the southwest the fault zone becomes increasingly complex and additional faults form part of the wider deformation of the region. This complexity has generated several different schemes for defining the number of segments and different names for the same structures, here we broadly follow the naming of fault strands proposed by Duman and Emre (2013). The multiple faults have also triggered debate as to the location of the triple junction between the EAFZ, DSFZ and the Cyprus Arc, with three main geodynamic models proposed. One model proposes that the EAFZ continues to the Mediterranean Sea in the south-west, crossing the Amanos Mountains to the Bay of İskenderun (e.g. Şengör and Yilmaz, 1981; Yönlü et al., 2017). This model would make the Amanos Fault Zone/-Karasu Rift the northern extent of the DSFZ with the triple junction in the vicinity of Türkoğlu (sometimes termed the Kahramanmaraş triple junction) between the Amanos Fault and the Pazarcık segment of the EAFZ. A similar model suggests that the EAFZ terminates at Türkoğlu and does not extend further to the SW (e.g., Perinçek and Çemen, 1990; Yürür and Chorowicz, 1998). By contrast, others (e.g., Arpat and Saroglu, 1972; Şengör et al., 1985; Duman and Emre, 2013) propose that the EAFZ continues south along the Amanos Fault and meets the DSFZ at the southern end in the Amik Plain. In this model the boundary of between the Anatolian and African plates is often placed through the Hatay Graben (Boulton et al., 2006; Boulton and Robertson, 2008) or along the Latakia Fault in northern Syrian (Hardenberg and Robertson, 2007).

Additional confusion arises from the fact that there are contrasting views on the position of the Cyprus Arc, generally considered to be the active plate boundary to the south of Cyprus accommodating convergence between Africa and Anatolia (Ben-Avraham, 1978; Kempler and Garfunkel, 1994). To the west and south of Cyprus the boundary is well defined; however, to the east this is not the case and there is no arc-trench system present. Different models suggest that there is no boundary in the area (Ben Avraham, 1978); that there are two boundary segments to the north and south Cyprus (Le Pichon and Angelier, 1979; Lort, 1971); that there is a broad zone of active convergence from Cyprus to the Iskenderun Basin towards the proposed Kahramanmaraş triple junction (Dewey et al., 1986; Dewey and Şengör, 1979; McKenzie, 1978); or that the arc is partitioned into a series of strike-slip systems forming a wide zone and not a discrete plate boundary (Kempler and Garfunkel, 1994; Robertson, 1998; Vidal et al., 2000).

2.2. Instrumental and historical seismicity

In historical times the city of Antakya was known as Antioch, one of the most important cities in the near eastern world, established ~300 years B.C.E (Before Common Era). As a result, historical records are particularly good for the coastal region, but fewer historical accounts are available for areas inland. Between the founding of Antioch and 1000 C.

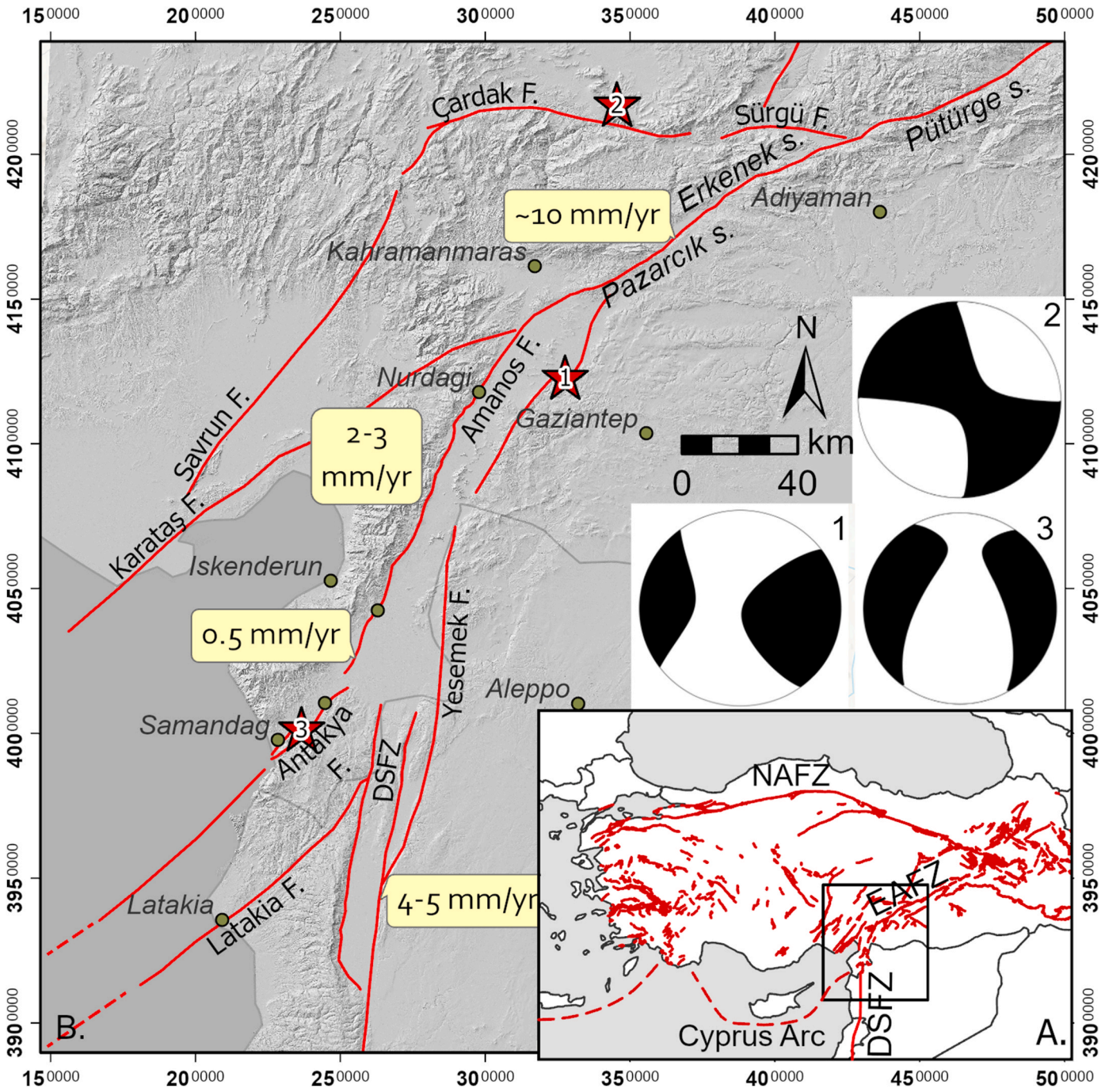

Fig. 1. A. Inset location map showing the active faults of Türkiye and surrounding region (adapted from Emre et al., 2018) and location of the main map, EAFZ – East Anatolian Fault Zone; NAFZ – North Anatolian Fault Zone, DSFZ – Dead Sea Fault Zone. B. showing detail of the active faults (adapted from Emre et al., 2018) and locations of the (1) Mw 7.8 Pazarcık and (2) Mw 7.5 Elbistan earthquakes including the significant Mw 6.4 aftershock that occurred near Antakya (3). Focal mechanisms plotted using the Matlab code of Conder (2024) with data retrieved from the AFAD-DDB earthquake catalogue. Base map is a hillshade derived from the ALOS World3D30 DEM ©JAXA projected in ED50 UTM Zone 37N. Note F = Fault; s = segment.

E. (Common Era) the area experienced approximately thirteen significant earthquakes (Ambraseys, 2009; Erol and Pirazzoli, 1992; Guidoboni et al., 1994). Historical records between the end of the 10th century and the 19th century are potentially less complete but contain more detailed information allowing the intensity of those earthquakes to be estimated. However, only one magnitude >7 event is recorded during this period along the EAFZ. The earthquake on the 29th November 1114 (Al-Tarazi, 1999; Ambraseys, 2009) ruptured the Pazarcık segment of the EAFZ (Carena et al., 2023), which is supported by recent palaeo-seismic trenching (Yönlü and Karabacak, 2024). This earthquake followed several smaller foreshocks that affected the wider region and resulted in significant loss of life; Ambraseys (2009) estimates a maximum intensity for the earthquake of VII (Fig. 2A) using the Medvedev-Sponheuer-Karnik (MSK) scale. Subsequently, several large earthquakes > M 7.0 took place along the DSFZ (Meghraoui et al., 2003). Like the 1114, the 1157 event (Fig. 2B) was preceded by at least a year of strong foreshocks culminating on August 12th, 1157. The precise location of this event is unclear with large amounts of damage suggesting an epicentre along the northern DSFZ (Guidoboni and Comastri, 2005) with a maximum intensity of X on the Mercalli Cancani Sieberg

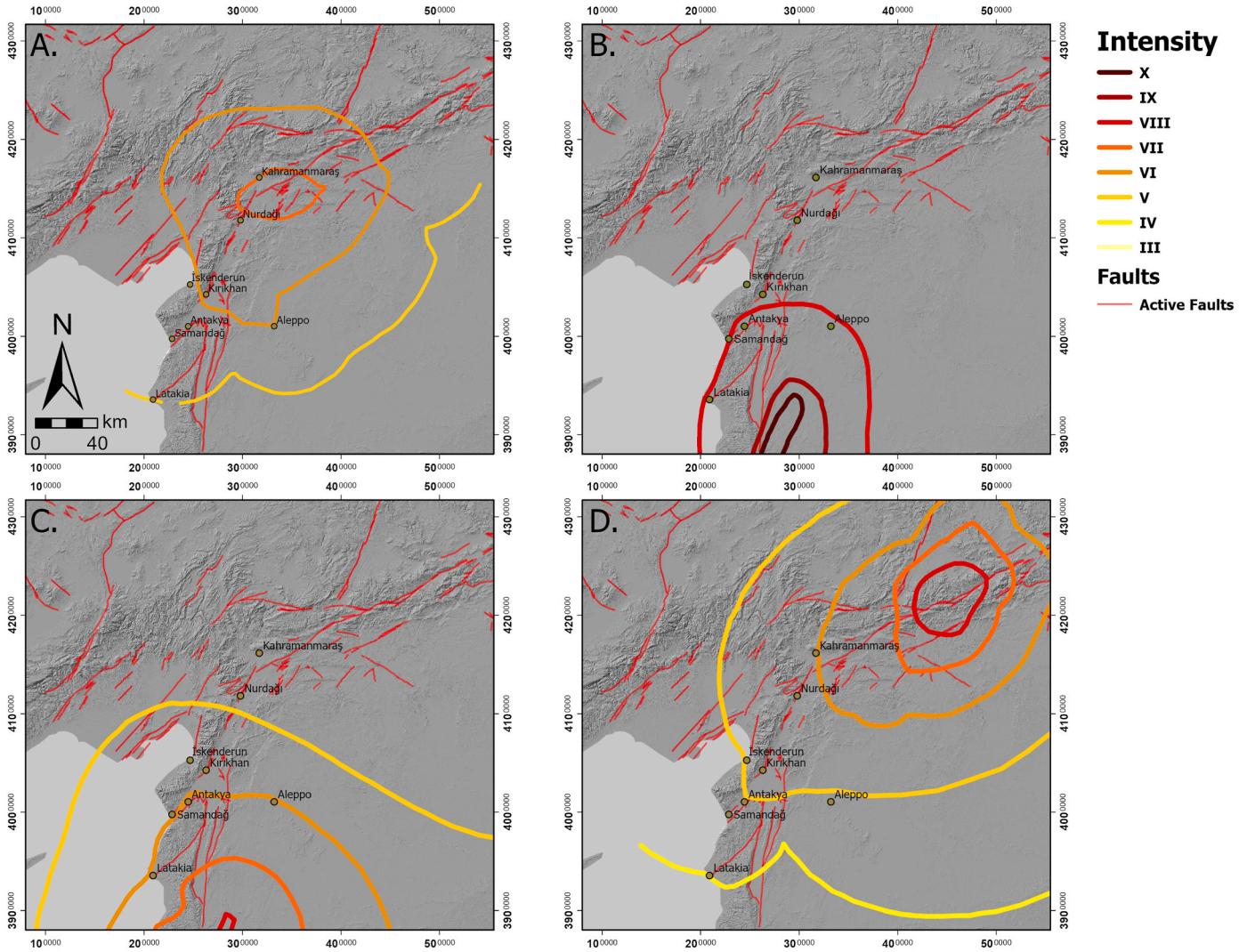

Fig. 2. *Isoseismal intensity maps for the strong earthquakes that occurred on A. 29*th *November 1114; B. 12*th *August 1157 (inferred using data from* Guidoboni and Comastri, 2005 *who used the* Mercalli Cancani Sieberg (MCS) intensity scale*); C. 29*th *June 1170 and D. March 2, 1893, A., C. and D. adapted from* Ambraseys (2009) *who used the* Medvedev-Sponheuer-Karnik (MSK) intensity scale. *The base map is a hillshade derived from the ALOS World3D30 DEM ©JAXA projected in ED50 UTM Zone 37N.*

(MCS) scale. Later earthquakes such as the 1170 (Fig. 2C) appear to have migrated further southwards along the DSFZ (Meghraoui et al., 2003).

By contrast, several large earthquakes >Mw 6.8 are known to have occurred during the 19th century in 1822, 1872, 1874, and 1893 along either the northernmost part of the DSFZ or rupturing individual segments of the EAFZ (Ambraseys, 2009; Duman and Emre, 2013; Carena et al., 2023) (Fig. 2D). For western Türkiye records of earthquakes of Mw > 6.8 are complete from 1800 (Stucchi et al., 2013); therefore, a similar date may also be applicable for southern Türkiye and these events may represent a full earthquake catalogue for this pre-instrumental period.

Recent instrumentally recorded seismicity has in general been characterised by shallow, small magnitude earthquakes. The most significant recent event was the Mw 6.8 Elazığ earthquake (January 24, 2020). This earthquake ruptured the Pütürge segment of the EAFZ for ~50 km with a maximum horizontal offset of ~2.4 m at 6–9 km depth (Pousse-Beltran et al., 2020). However, there was no surface deformation (Çetin et al., 2020) consistent with modelled slip deficit (Pousse-Beltran et al., 2020). Interestingly, this section of the EAFZ had been previously proposed as a potential seismic gap by Duman and Emre (2013), though high numbers of small to medium earthquakes in the decades prior to the Elaziğ earthquake argue against that interpretation (Bulut et al., 2012; Pousse-Beltran et al., 2020).

2.3. Geology and seismology of the Kahramanmaraş earthquakes

Six faults/fault segments ruptured during the Kahramanmaraş earthquake sequence; these were the Narlı Fault, the Erkenek and Pazarcık fault segments of the EAFZ, and the Amanos Fault during the Pazarcık earthquake and subsequently the Çardak Fault and possibly the Sürgü Fault during the later Elbistan event (Fig. 1).

The Pazarcık earthquake is characterised by four phases (i.e., Jia et al., 2023; Okuwaki et al., 2023; Petersen et al., 2023). In phase I, the Narlı Fault and Pazarcık and Erkenek segments of the EAFZ rupture. The Narlı Fault, a relatively unknown structure forming the eastern margin of a small basin, appears to be the structure that initiated the Mw 7.8 Pazarcık earthquake (Melgar et al., 2023). The fault is oblique normal with evidence of Late Quaternary-Holocene fault activity in the form of prominent fault scarps (Duman and Emre, 2013). The Pazarcık and Erkenek segments are sinistral strike-slip faults of the EAZF separated by the Gölbası Basin (a pull-apart basin). The Erkenek segment is ~30 km long with up to 26 km of offset, whereas the Pazarcık segment is longer at > 50 km but also has up to 25 km of offset (Duman and Emre, 2013). In this phase, the rupture propagated unilaterally ~130 km in a NE

direction in ~40 s (Petersen et al., 2023).

Subsequently, in phase II at ~50 s after the earthquake nucleation, the rupture propagated bilaterally further northwards along the Pazarcık and Erkenek segments but also southwards along the Amanos Fault. The Amanos Fault forms the western margin of the Karasu Rift, again a sinistral strike-slip fault but with an earlier history of extension resulting in the uplift of the Amanos Mountains (Boulton, 2009, 2013). The fault has a number of sections along its ~125 km length with a reported maximum displacement of 700 m (Boulton, 2013) and a horizontal slip rate of ~3 mm/yr (Seyrek et al., 2007). In the final two phases of the Pazarcık earthquake, the rupture continues unilaterally to the SW through the Hatay Graben and finally offshore (Petersen et al., 2023).

The Pazarcık earthquake generally occurred at shallow depths (8.6–10.0 km) (Petersen et al., 2023) with maximum rupture speeds of up to 3.2–3.4 km/s, for a total duration of 80–117 s; therefore making this a supershear earthquake (Karabulut et al., 2023; Melgar et al., 2023; Petersen et al., 2023).

The later Mw 7.5 earthquake primarily ruptured the Çardak and Sürgü faults, which previously had been proposed to be a northern strand of the EAFZ (Duman and Emre, 2013). The Çardak Fault is a sinistral strike-slip fault that has a reported length of 85 km and maximum offsets of 135 m with an estimated Holocene slip-rate of 2.5 mm/yr (Duman and Emre, 2013). This second earthquake occurred in a single phase with rupturing taking place bi-laterally to the west and then to the east over 115–150 km (Melgar et al., 2023; Okuwaki et al., 2023; Petersen et al., 2023). Melgar et al. (2023) state the westwards rupture was supershear reaching 4.8 km/s, although this velocity is higher than values derived by Petersen et al. (2023) of 3.2 km/s, while eastwards rupture speeds were sub-supershear at 2.8 km/s (Melgar et al., 2023).

Although the Elbistan earthquake occurred 9 h after the Pazarcık earthquake, these two events can be considered as a doublet earthquake rather than a main shock and aftershock event, as there is < 1.2 Mw difference between the size of the earthquakes (Goldberg et al., 2023). Following these mainshocks there were thousands of aftershocks recorded in the region (Fig. 3; Lomax, 2023). The most significant of these was the Mw 6.4 Antakya aftershock (also known as the Uzunbağ earthquake) on the February 20, 2023 near the southeastern-most extent of the Pazarcık rupture in the Hatay Graben, on a fault-striking 237 ± 5°and dipping at 55 ± 5° (Barbot et al., 2023) with dominantly normal dip-slip displacement (Fig. 1).

3. Methods

The Earthquake Engineering Field Investigation team (supported by the UK's Institution of Structural Engineers, IStructE) is a collaboration since 1984 between academia and industry to collect data primarily on the built environment response but also on the natural environment response following major earthquakes. Following the 6th February earthquakes, a hybrid mission using both traditional field techniques and remote sensing data analysis was mobilised to gather information on aspects of the event such as the seismotectonics, geotechnics, building and infrastructure damage, and relief, response and recovery (Aktas et al., 2024) following approaches developed in previous hybrid EEFIT missions (e.g., Aktas et al., 2022; Whitworth et al., 2022).

As part of this mission, data were required on the EEEs resulting from the earthquake as well as an understanding of the distribution of strong ground shaking in such a geologically complex region. Remote sensing observations and measurements of primary and secondary EEEs where derived from high-resolution satellite imagery provided to the scientific community as part of the disaster response with processing undertaken in ArcGIS Pro. This data not only provides critical information to guide the subsequent field investigations but also enables data collection over a much greater area than possible during relatively short field missions. Analysis of the Turkish ground motion network was also undertaken to provide context for the observations made in the field.

Analysis-ready data provided through the Maxar Open Data programme with a spatial resolution of ≤0.5 m was acquired for the mapping and measurement of surface ruptures along the fault trace of the Amanos and Narli faults and the Pazarcık and Erkenek segments of the EAFZ. Similar high-resolution imagery is not available for the Çardak and Sürgü Faults, therefore the data coverage is not complete (Supp. Fig. 1).

The Maxar imagery was also used for the localised mapping of other EEEs resulting from the earthquake including landslides, rockfalls, and areas affected by intense liquefaction and lateral spreading. These features were mapped manually as points using visual comparison between pre- and post-event images. As discussed later in this paper, the localised mapping undertaken by EEFIT for landsliding/rockfalls, and liquefaction was then combined with other regional-scale datasets of these EEEs in the literature to produce comprehensive event inventories. ArcGIS Pro spatial analysis tools were then used to create kernel density maps showing the overall spatial distributions of these EEEs across the study area considered in this paper.

Following the remote data collection phase, a 1 week field mission was undertaken to gain field validation of remotely sensed observations and collect primary data. The team obtained permission from local authorities to visit the affected areas in Türkiye and the field visit was undertaken by a field team of 15 people over the period 13–17th March 2023. Unfortunately, visiting locations in Syria was not possible owing to the political situation. While the focus of the missions was primarily on the built environment, valuable insights and observations were additionally made on environmental changes (Aktas et al., 2024).

4. Strong ground motion

Türkiye has an extensive ground motion network, including in the regions effected by the earthquakes, which serve as part of the Turkish Accelerometric Database and Analysis System (TADAS), which is managed by AFAD, the Disaster and Emergency Management Presidency which operates under the Ministry of the Interiors. In addition, Kandilli Observatory and Earthquake Research Institute (KOERI) of Boğaziçi University operates several additional stations. Unfortunately, ground motion data was not available from Northwestern Syria despite the Kahramanmaraş earthquake sequence's serious impacts. Within 300 km of the epicentral distance, strong ground motions recorded by both Turkish networks were examined as part of the EEFIT mission. First, unusable strong ground motion recordings, which did not meet the initial quality requirements such as those with noticeable noise contamination and time series interruptions, were discarded. After that, undesired noise was eliminated from the remaining raw ground motions to enhance their quality. This processing involved applying baseline corrections and 4th-order Butterworth bandpass filtering. The completed database comprised strong ground motion recordings from 128 stations for the Pazarcık Earthquake (Mw 7.8) and 154 stations for the Elbistan Earthquake (Mw 7.5).

In the initial evaluation of the shaking intensity, peak ground acceleration (PGA) typically serves as one of the most prevalent metrics, assessed in relation to distance and local site conditions. Hereafter, PGA will denote the resultant peak ground acceleration, representing the absolute maximum of the acceleration time series, determined by the square root of the sum of the squares of transverse components.

PGAs were at highest levels for both earthquakes at the seismic stations in proximity to the fault ruptures (near-fault areas), which passed through the cities of Adıyaman, Kahramanmaraş, Gaziantep, and Antakya in the case of the Mw 7.8 Pazarcık event, and exclusively Kahramanmaraş and Malatya for the Mw 7.5 Elbistan event (Fig. 1).

For the Mw 7.8 Pazarcık earthquake, all seismic stations with PGAs exceeding 1g were situated within the Amik Basin of Hatay, where the city of Antakya was profoundly impacted by the shaking. The highest PGA detected was 1556 cm/s^2 at station 3129, positioned roughly 139 km from the epicentre of the earthquake (Fig. 3A). Even though the average shear wave velocity (VS30) at station 3129 was approximately

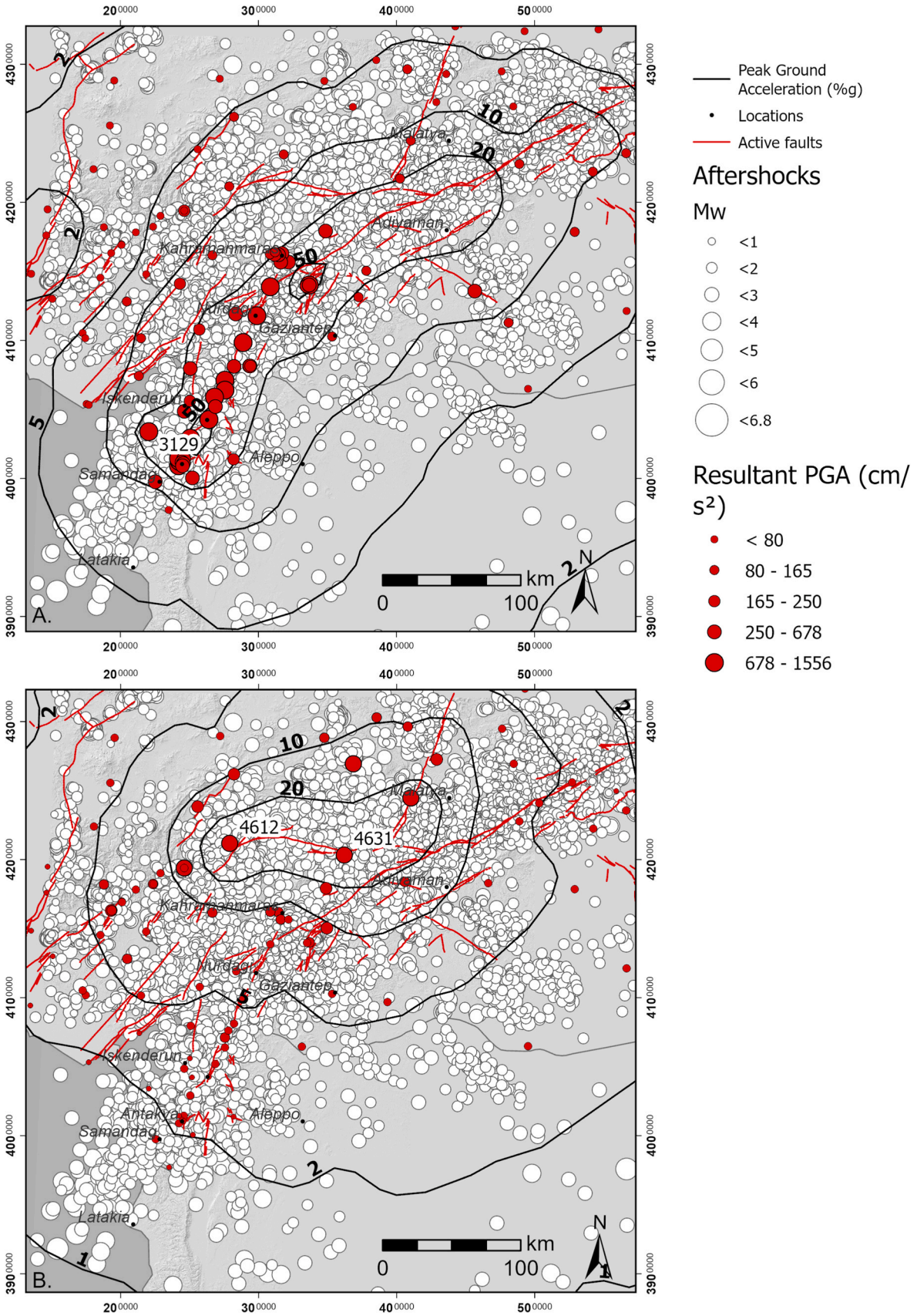

Fig. 3. *Map of Peak Ground Acceleration (PGA) from USGS (lines) and from the TADAS and KOERI monitoring networks (points) for the A)* Pazarcık *and B) Elbistan events shown with aftershock data catalogue from* Lomax (2023). *Base map is a hillshade derived from the ALOS World3D30 Dem ©JAXA projected in ED50 UTM Zone 37N.*

447 m/s within the top 30 m, classifying the site as ZC soils (indicative of very dense sand, gravel, and very stiff clay or weathered, highly fractured weak rocks, c.f., soil category B in Eurocode 8) according to the existing seismic regulation of Türkiye (TBEC, 2018), the potential effects of the basin nonetheless played a significant role in the observed large PGAs (Aktas et al., 2024). Furthermore, Amik Basin stations were situated on the southwestern side of the fault rupture, at a Joyner-Boore (JB) distance of 0.4 km from the fault, while being a comparatively considerable distance from the epicentre.

The Mw 7.5 Elbistan earthquake caused the most severe impact on the northern regions of the earthquake-affected zone, specifically the northern districts of Kahramanmaraş and the southern provinces of Malatya. Stations 4612 (JB Distance ≈ 0 km; VS30 ≈ 246 m/s) and 4631 (JB Distance ≈ 1.9 km; VS30 ≈ 543 m/s) were situated near the fault rupture (Fig. 3B) and on the sites characterised by ZD (medium-dense/dense sand, gravel, or very solid clay) and ZC soil classes of TBEC (2018), respectively. Station 4612, located at the western extremity of the fault rupture, registered the highest PGA at 678 cm/s^2 whereas station 4631 exhibited a relatively lower PGA of 463 cm/s^2.

5. Earthquake environmental effects

5.1. Primary effects (Surface rupture and uplift/subsidence)

The Turkish earthquakes resulted in surface ruptures of >350 km in length along the EAFZ and >150 km in length along the Çardak-Sürgü Fault (Fig. 4). These surface ruptures were a focus of observation and measurement following the event with some early field campaigns in the region taking place within 10 days of the event (e.g., Karabacak et al., 2023; Kozaci et al., 2024; Kurcer et al., 2023; Moss et al., 2024; Softa et al., 2024). Similarly, optical offset tracking (Barbot et al., 2023; He et al., 2023; Mai et al., 2023; Provost et al., 2024), InSAR processing (Atanasova et al., 2023; Kobayashi et al., 2024; Li et al., 2023, 2024; Mikhailov et al., 2023; Ou et al., 2023) and remote sensing observations of the rupture covering regions of the fault trace (e.g., Guo et al., 2023; Reitman et al., 2024) using high-resolution satellite imagery, provide further constraints on the magnitude of the displacement and complement the field observations.

Surface rupture maps were quickly released after the earthquake (i.e., Reitman et al., 2024) and have been supplemented by extra mapping along the EAFZ as part of this study (Fig. 4). This updated fault trace includes the addition of previously unmapped faults to the previously published dataset and dataset validation, resulting in the removal misidentified fault structures where features were recognised to be the result of either crop marks, such as old field boundaries, tractor marks, buried/ancient channels, forest tracks, or the shadow of telegraph poles. Supplementary high-resolution mapping was not possible along the Çardak-Sürgü Fault as the region was not covered by data released through the Maxar Open Data Programme, although this fault has been investigated in the field by Softa et al. (2024).

Both in the field and on remote sensing imagery, surface ruptures can be recognised through a series of features that cut and offset man-made features such as roads, buildings, railways, field boundaries, and canals, and also disrupt natural features such as rivers and the ground surface (Fig. 5). This is because strike-slip nature of the faults can be easily recognised by the lateral offset of surface features. These piercing-points indicate that along all ruptured fault segments there is substantial variation in the lateral displacement (Figs. 4 and 6).

On the EAFZ maximum offsets derived from measurements of offset features in either the field or on high-resolution satellite imagery indicate maximum horizontal displacements (D_{max}) < 8 m (Fig. 6A). For example, Karabacak et al. (2023) report a D_{max} of 7.3 m, while the D_{max} of Kurcer et al. (2023) is 4.5 m, which is slightly smaller than the D_{max} mapped here of 5.1 m. In addition to lateral offsets, in the field the rupture can be observed to have highly variable vertical offsets. Although, at the majority of locations no vertical displacement is observed, Kurcer et al. (2023) recorded vertical offsets up to 0.9 m in the SE of the rupture zone (Fig. 7). Karabacak et al. (2023) recorded even larger vertical offsets particularly in the north of the study area, where they reported vertical offsets up to 1.6 m.

In contrast to the field observations, automated pixel tracking and InSAR-derived displacement measurements suggest greater and less variable offsets along the EAFZ than point observations, as these measurements may include off fault deformation. This includes estimations of the D_{max}, which is determined by Provost et al. (2024) to exceed 12 m in the north of the fault zone. Similarly, estimates of vertical displacement from InSAR are highly variable along strike with maximum uplift and subsidence values of 20–30 cm (Nofl et al., 2023; Kobayashi et al., 2024). Slip profiles (Fig. 6) reveal increases from minima at fault tips to maxima in the Pazarcık segment of the EAFZ Fault.

Several locations along the Pazarcık fault rupture were visited by the EEFIT field team. Near Ishahiye, the surface rupture was observed in fields and offsetting small drainage features (Fig. 8). Interestingly, where the main rupture appeared constant in the satellite imagery, field observations showed that at higher resolution the rupture was composed of a series of *en-echelon* linear segments (e.g., Fig. 8B). Ground fractures were also observed along an adjacent hillside (Fig. 8C), although it is unclear if these were primary fault surface rupture or gravity-driven fracturing similar to sackungen, which have been described elsewhere in Türkiye (Karasözen et al., 2016). Further north, surface rupture observations were made by the field team around the town of Gölbaşı (e.g., Fig. 8D), characterised by a step-over in the EAFZ. Here multiple surface ruptures were identified with a strike at a high angle to the main trend of the fault zone. It was also observed that these cracks diverted around building foundations in many cases, as a result it is unclear if these features are the primary surface rupture or secondary cracks.

Fewer investigations have been undertaken along the Çardak Fault, with Softa et al. (2024) presenting the only complete database of field-derived measurements (Fig. 6B). Their measurements suggest that the D_{max} = 6.6 m, conversely the field mapping of Kozaci et al. (2024) recorded a D_{max} of 8.6 m, while automated methods that suggest maximum displacements in the range of 7.5 m (Ou et al., 2023). Softa et al. (2024) also present data on vertical offsets, which again are mostly zero or negligible apart from at a few locations were significant (up to 3 m) vertical offsets can be observed.

5.2. Secondary environmental effects

5.2.1. Landslides/rockfalls/slope movements

Owing to the proximity of the main fault ruptures and areas of intense ground acceleration to steep mountainous terrain, landslide events (including rockfalls) were a concern following the earthquake sequence. Indeed, the USGS probabilistic Ground Failure model (Allstadt et al., 2022) near immediately produced the highest possible alert level (red) for landsliding for both earthquakes that made up the doublet sequence (Görüm et al., 2023).

As such, several studies, including EEFITs, had a focus on landslides in the immediate aftermath of the event (e.g., Görüm et al., 2023; Adamidis et al., 2023). One reason for this is that landslides can be a major hindrance to immediate post-earthquake response due to the blocking of vital transport networks such as roads and paths needed by emergency responders and aid workers (e.g., Jones et al., 2020; Kargel et al., 2016). Furthermore, landslides can also present significant ongoing hazards in the medium to long term. For example, initially incipient tension cracks and unseen landscape damage can lead to increased landslide activity during subsequent triggering events (e.g., Jones et al., 2021; Marc et al., 2015; Parker et al., 2015). In addition, landslides can generate hazard cascades such as outburst floods (e.g., Martha et al., 2015) through the creation of landslide dams. Indeed, in this case, a major valley-blocking landslide was observed by EEFIT (Adamidis et al., 2023) and Tobita et al. (2024) along Degirmencik Creek near the town of İslahiye, which resulted in the development of a

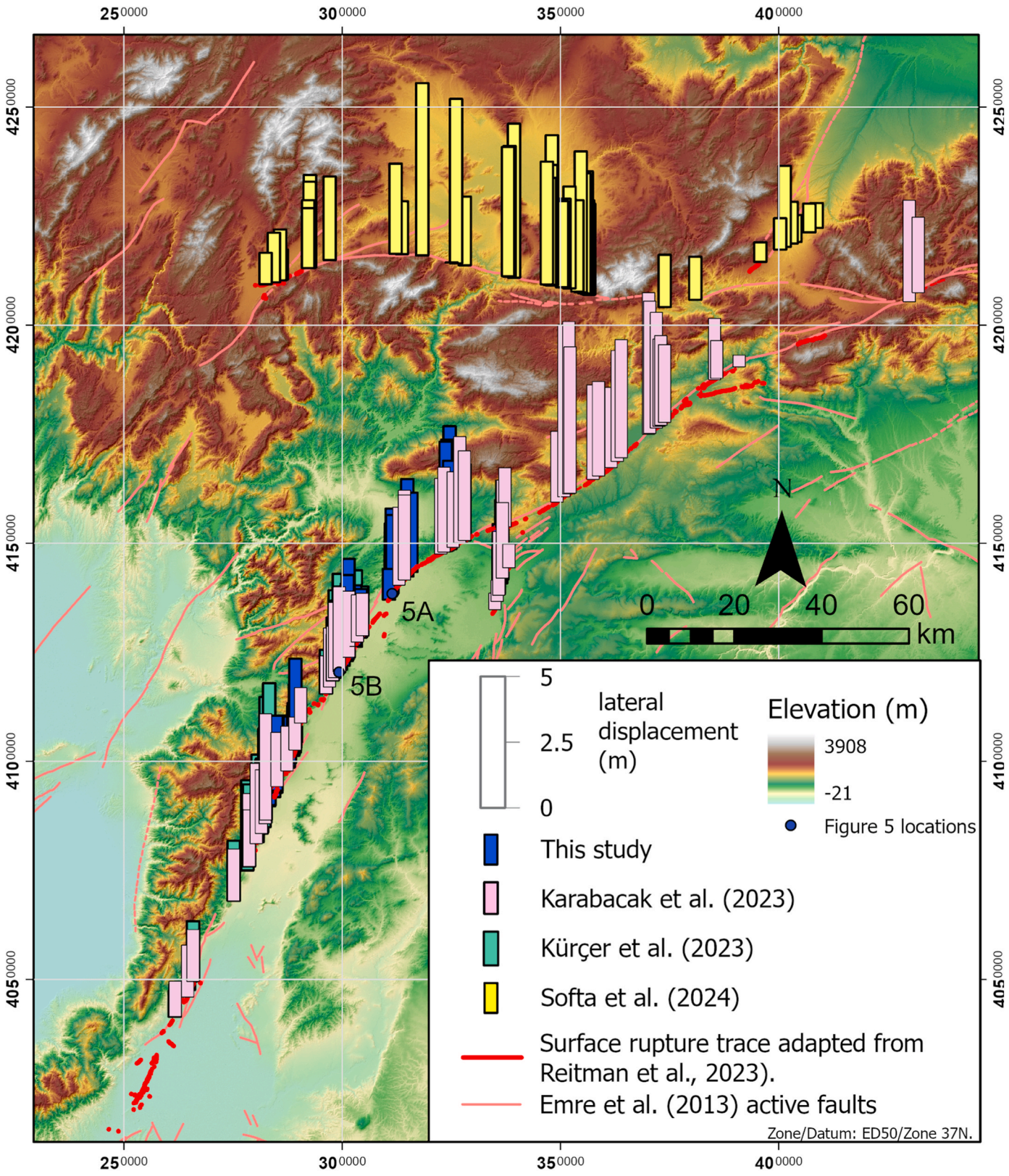

Fig. 4. *Map showing the measured horizontal offset from field and remotely sensed imagery across the region of surface faulting, data from* Karabacak et al. (2023); Kurcer et al. (2023); Softa et al. (2024) *and this study, alongside visible surface rupture trace derived from satellite image analysis. Base map is the ALOS World3D30 Dem ©JAXA projected in ED50 UTM Zone 37N. Note: all bars plotted using the scale shown.*

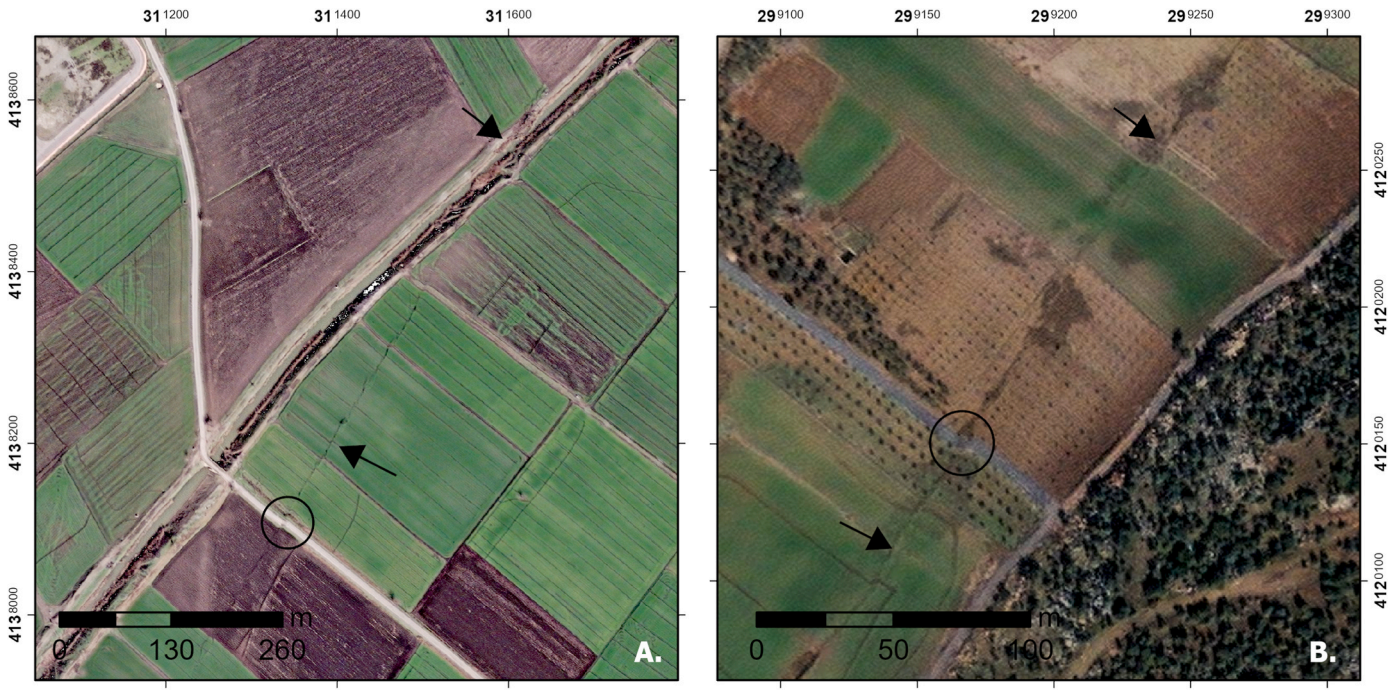

Fig. 5. Examples of the high resolution MAXAR imagery released through the Open Data programme showing examples of the geometry of the surface rupture. A) Offset fields, road and canal east of Türkoğlu; B) North of Nurdağı the rupture can again be traced through offset farm tracks and field boundaries. Locations of both areas is shown on Fig. 4.

lake upstream of the ~40 m high landslide dam (Fig. 9A and 10A). This landslide is 480 m long with an estimated volume of 996,000 m^3 (Tobita et al., 2024). However, the largest landslide to have occurred as a result of the earthquakes was observed to the east of Antakya, near the village of Tepehan, where a 496 m long landslide with an estimate volume of 1.1 million m^3 (Sümer, 2024; Tobita et al., 2024) failed in Middle-Upper Miocene limestones and marls (Fig. 9B).

Sümer (2024) and Tobita et al. (2024) only undertook analysis of individual landslide occurrences; the most comprehensive landslide study for the Kahramanmaraş earthquake sequence to date is that presented by Görüm et al. (2023). In this paper, the authors used a remote sensing approach utilising a range of optical satellite products combined with three weeks of detailed field validation to map 3673 landslides (as points) within an ~45,000 km^2 area bounded by the USGS 0.12 g PGA contour. This PGA contour was used to bound the mapping area as studies have shown that ~90 % of coseismic landslides typically occur at PGA occurrences greater than this acceleration (Tanyaş and Lombardo, 2019).

Spatial analysis of the co-seismic landslide inventory showed that >70 % of the mapped landslides occurred where PGA ranged from 0.3 to 0.6 g and on slopes with elevations of 800–1400 m, angles of 20–45°, south-facing aspects, and local reliefs of 400–700 m (Görüm et al., 2023). In terms of geology, landslides were found to be preferentially occurring within metamorphic and ophiolitic rocks, with schist, gneiss, and pelagic limestone the most landslide-susceptible units (Görüm et al., 2023). The majority of landslides in the inventory were assessed as being rockfall events (i.e., Fig. 10), with some events observed to have runout distances of over 600 m from their source zones; bedrock rotational slides, translational slides, and lateral spread-type failures were also observed (Görüm et al., 2023).

Here, the inventory produced by Görüm et al. (2023) is combined with the localised landslide inventory produced by the EEFIT mission. In total, the EEFIT team mapped 304 co-seismic landslides, predominantly in the Amanos Mountains to the south, east, and northeast of Iskenderun, and the area around the town of İslahiye. Of these 304 landslides, 189 had not been mapped as part of the Görüm et al. (2023) inventory, leading to a combined total inventory of 3826 landslide events. This combined inventory (Fig. 11) shows that landslides are spatially distributed all along the main fault rupture, with high density zones in the Amanos Mountains to the southwest and in the mountains to the east/northeast of each earthquake epicentre. There is also a high-density zone to the west of the second Mw 7.5 earthquake epicentre.

5.2.2. *Liquefaction and lateral spreading*

Liquefaction is a process whereby earthquake induced strong ground motions cause cohesionless partially water-saturated sediments to temporarily lose strength and stiffness and behave like a fluid (Youd, 1973). If the liquefied sediments are unconstrained (e.g. they form part of a riverbank or embankment) then this can cause a process caused lateral spreading, where the ground physically moves laterally towards the unconstrained direction (Cubrinovski and Robinson, 2016). This can result in large ground fissures and significant damage to infrastructure. Liquefaction can also cause severe settlement or subsidence to structures founded within liquefied material (Tsukamoto and Ishihara, 2010; Chang et al., 2012).

In the case of this event, evidence of liquefaction induced damage was quickly reported by early responders, including both EEFIT and GEER (Geotechnical Extreme Events Reconnaissance (Moss et al., 2024)), particularly around Gölbaşı, the Orontes/Asi River near Antakya, and in the fishing port and town of Iskenderun (Adamidis et al., 2023; Cetin et al., 2023a). Owing to time constraints, EEFIT decided to undertake detailed mapping with MAXAR imagery of liquefaction and lateral spreading extents in the Orontes/Asi River and Iskenderun regions only, with 457 instances of liquefaction and/or lateral spreading identified in these areas. The mapping focused on identifying typical liquefaction evidence such as circular sand boils or linear fissures both of which are common manifestation of liquefaction ejecta and parallel ground cracks/fissures that mark the extents of lateral spreading. This mapping shows that the liquefaction damage is strongly controlled by geomorphology, where flood plains with meandering river networks and lacking constrained surfaces suffering heavy damage. For example, the damage caused by lateral spreading in the meander loops of the

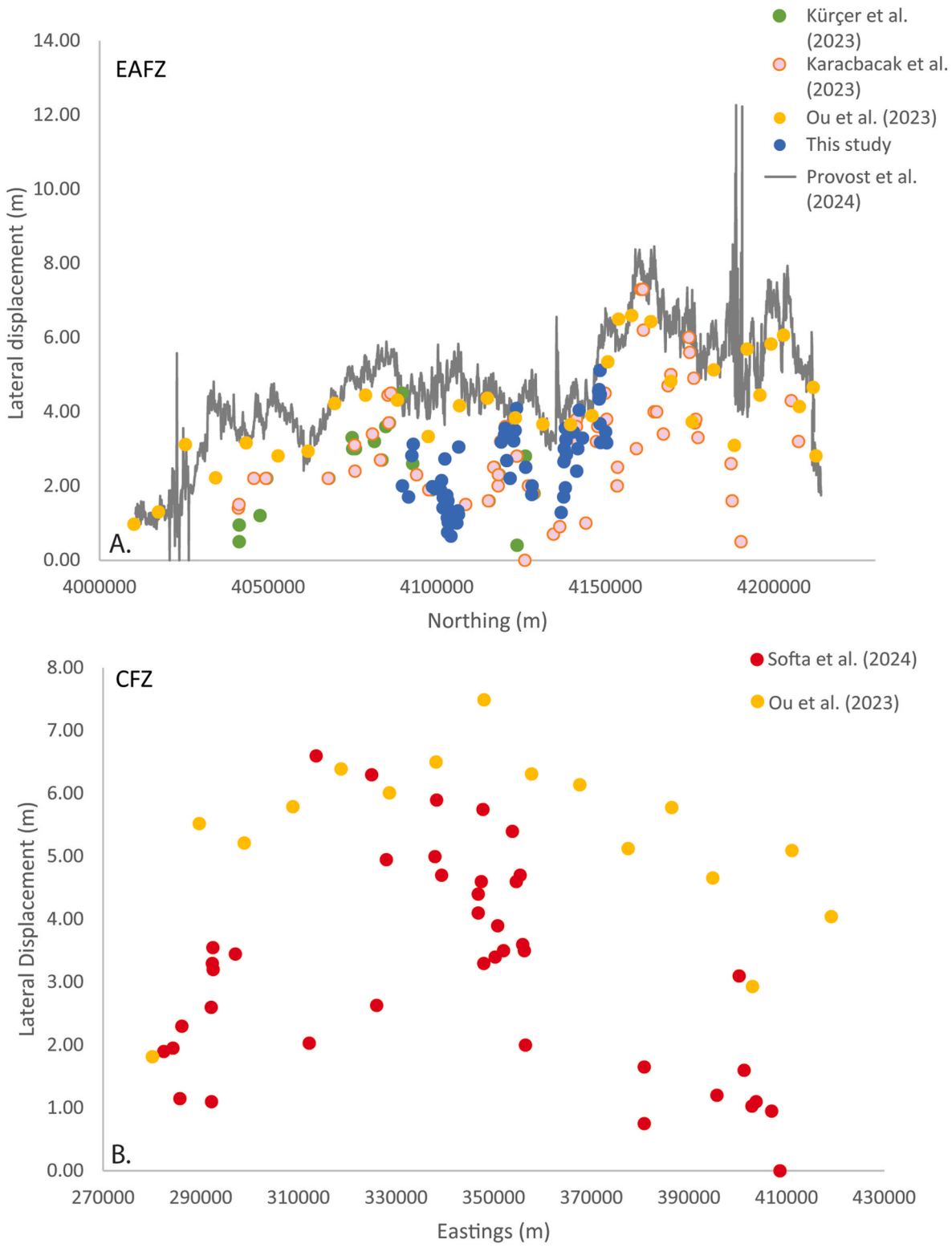

Fig. 6. *Comparison between lateral offsets measured from field, remote sensing and automated extraction methods for A. the EAFZ and B. the* Çardak *Fault. Note x-axis are plotted using UTM distances thus allowing for data from difference studies to be plotted together where the* 0 km *point of along strike-distances is not stated. Data from* Karabacak et al. (2023); Kurcer et al. (2023); Ou et al. (2023); Provost et al. (2024); Softa et al. (2024).

Orontes/Asi River region was intense, with multiple occurrences of damaged buildings and roads (Fig. 12).

Liquefaction and lateral spreading were also studied by Taftsoglou et al. (2023), who undertook detailed mapping across the entire earthquake affected area using remote sensing methods. Their remote sensing approach was phased, with multiple optical datasets used to visually identify and map liquefaction and associated features. The imagery used included Sentinel-2, Planet Labs (Planetscope and SkySat), Maxar, GeoEye-1, WorldView 1-2-3, orthophotos made available by the Turkish Ministry of National Defence General Directorate of Mapping, and

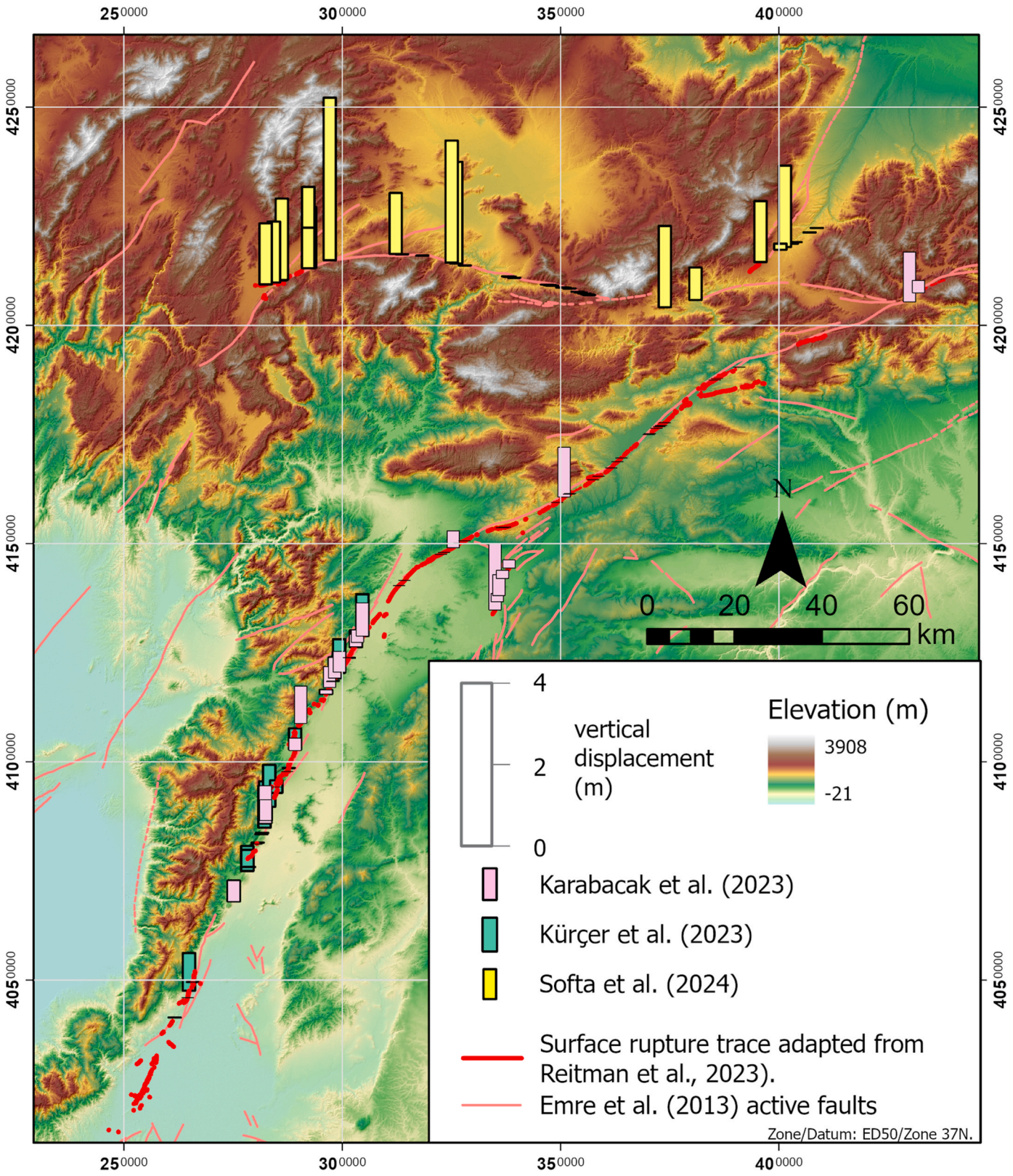

Fig. 7. *Map showing the measured vertical offset from field and remotely sensed imagery across the region of surface faulting, data from* Karabacak et al. (2023); Kurcer et al. (2023); Softa et al. (2024) *alongside visible surface rupture trace derived from satellite image analysis. Base map is the ALOS World3D30 Dem ©JAXA projected in ED50 UTM Zone 37N. Note: all bars plotted using the scale shown.*

Fig. 8. Field photographs of the surface rupture from the vicinity of İslahiye, A) close-proximity rupture across a grass field (37 3 36.07 N; 36 37 4.75 E); B) view of surface rupture with en echelon or Riedel shear characteristics (37 3 35.04 N; 36 37 4.59 E). C) ground cracks on hillside nearby at (37 3 32.13 N; 36 36 55.81 E) D) Example of surface rupture with vertical offset further to the north near Gölbası (37 49 56.05 N; 37 43 40.25 E).

additional UAS orthophoto surveys published through the Open-AerialMap Portal. To help constrain the mapping, they focused on the area enclosed by the 0.1 g USGS ShakeMap PGA contour, as previous experience suggests that this is the PGA required for liquefaction to occur in this geology (Papathanassiou et al., 2022). In total, Taftsoglou et al. (2023) mapped 1850 sites of liquefaction and/or lateral spreading. Overall, they found that the 95th percentile of all liquefaction sites correspond with PGA >0.14 g and PGV >12 cm/s, suggesting that these seismic values could be a good early predictor for earthquake environmental effects in such events (Taftsoglou et al., 2023). Their study also noted the importance of geomorphology in controlling liquefaction, with river meanders, paleo-channels, point-bar formations, abandoned and infilled rivers, floodplain valley/basins, drained basins (with Holocene lacustrine and fluvial deposits), and coastal zones being most intensely affected.

To fully characterise the extent of lateral spreading for this event, the liquefaction/lateral spreading inventories made by EEFIT and Taftsoglou et al. (2023) are combined. Of the 457 instances mapped by EEFIT, 200 were not mapped by Taftsoglou et al. (2023), leading to a final liquefaction/lateral spreading inventory of 2050 features. This combined inventory is shown in Fig. 13 alongside a liquefaction/lateral spreading Kernel Density map produced using ArcGIS Pro. This shows that liquefaction and lateral spreading is concentrated to the southwest of the first earthquake around Iskenderun and the Orontes/Asi River, and to the north and northwest/northeast of the first earthquake in the region between Gaziantep and Kahramanmaraş. The second earthquake does not seem to have caused significant liquefaction. As outlined by Taftsoglou et al. (2023), the clearest control on the distributions of liquefaction and lateral spreading is geomorphologically controlled superficial geology, with the affected areas predominantly comprising relatively unconsolidated and saturated Holocene and Plio-Quaternary riverbeds, river terraces, flood plains, and lacustrine and coastal deposits. This would explain why there was less liquefaction associated with the second earthquake, as this event occurred at a higher latitude in

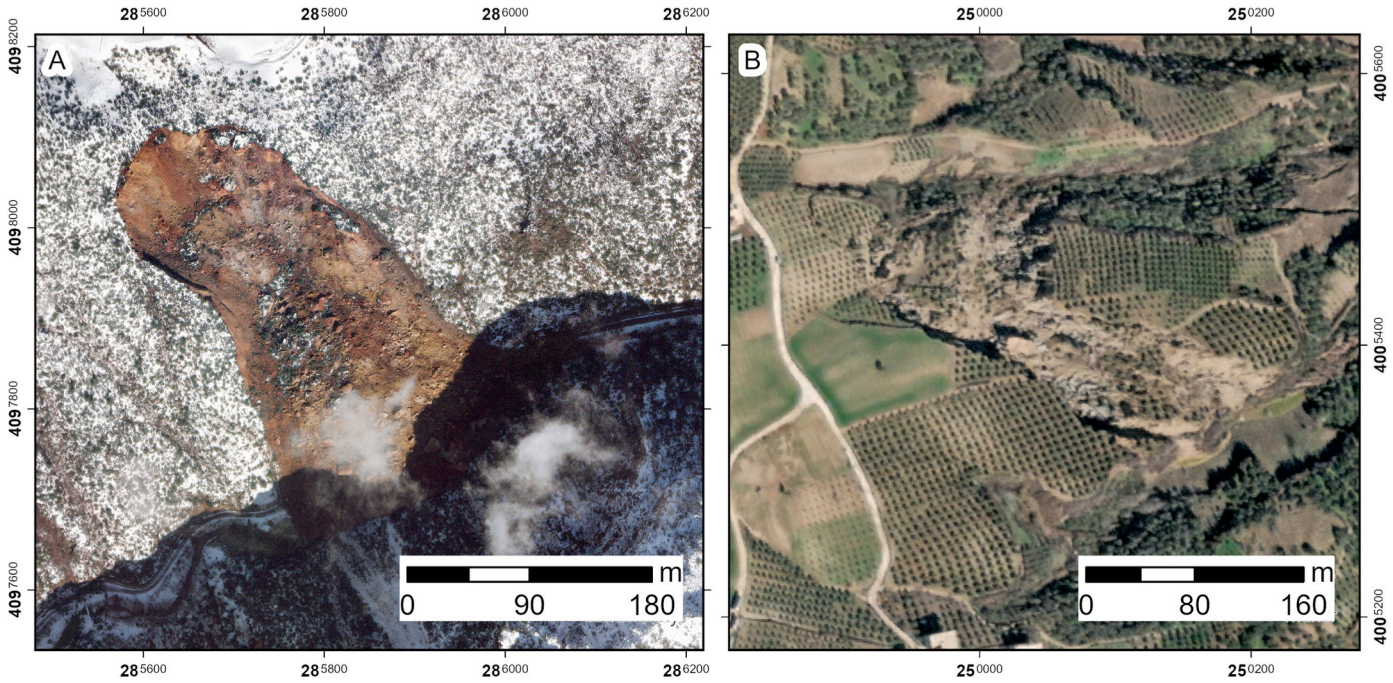

Fig. 9. A. The large landslide SW of Islahiye shortly after the earthquake (7th February) that subsequently resulted in the formation of a landslide lake. Image source: MAXAR Open Data Programme. B) The Tepehan slide to the SE of Antakya. Image source: ESRI World Imagery.

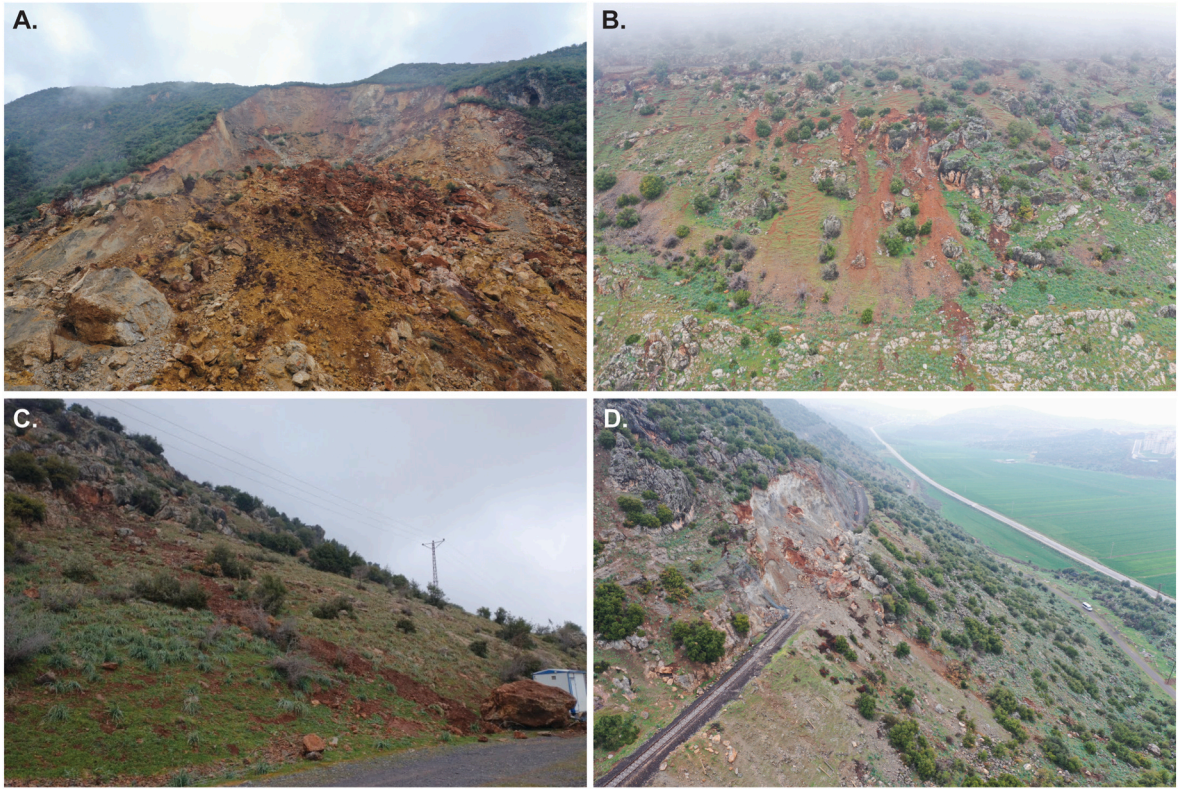

Fig. 10. A) View of the large landslide *SW of Islahiye* (Fig. 8A*) from the ground (taken from 37 0 2.27 N; 36 35 40.21 E); B) and C) UAV and ground perspective of rockfalls effecting a local road and water infrastructure at 37 5 19.78 N; 36 38 1.82 E; note powerlines in bottom left of B that can also be seen in C., and D) UAV view of a shallow landslide that blocked rail infrastructure at 37 4 58.50 N; 36 37 36.92 E.*

an area dominated by hard-rock bedrock geology.

5.2.3. *Tsunami warnings and inundation effects*

Despite the Mw 7.8 Pazarcık earthquake occurring nearly 100 km inland, the Intergovernmental Oceanographic Commission - United Nations Educational, Scientific and Cultural Organization (IOC-UNESCO) for the Northeast Atlantic, Mediterranean, and connected seas Tsunami Warning System (NEAMTWS) responded promptly offering

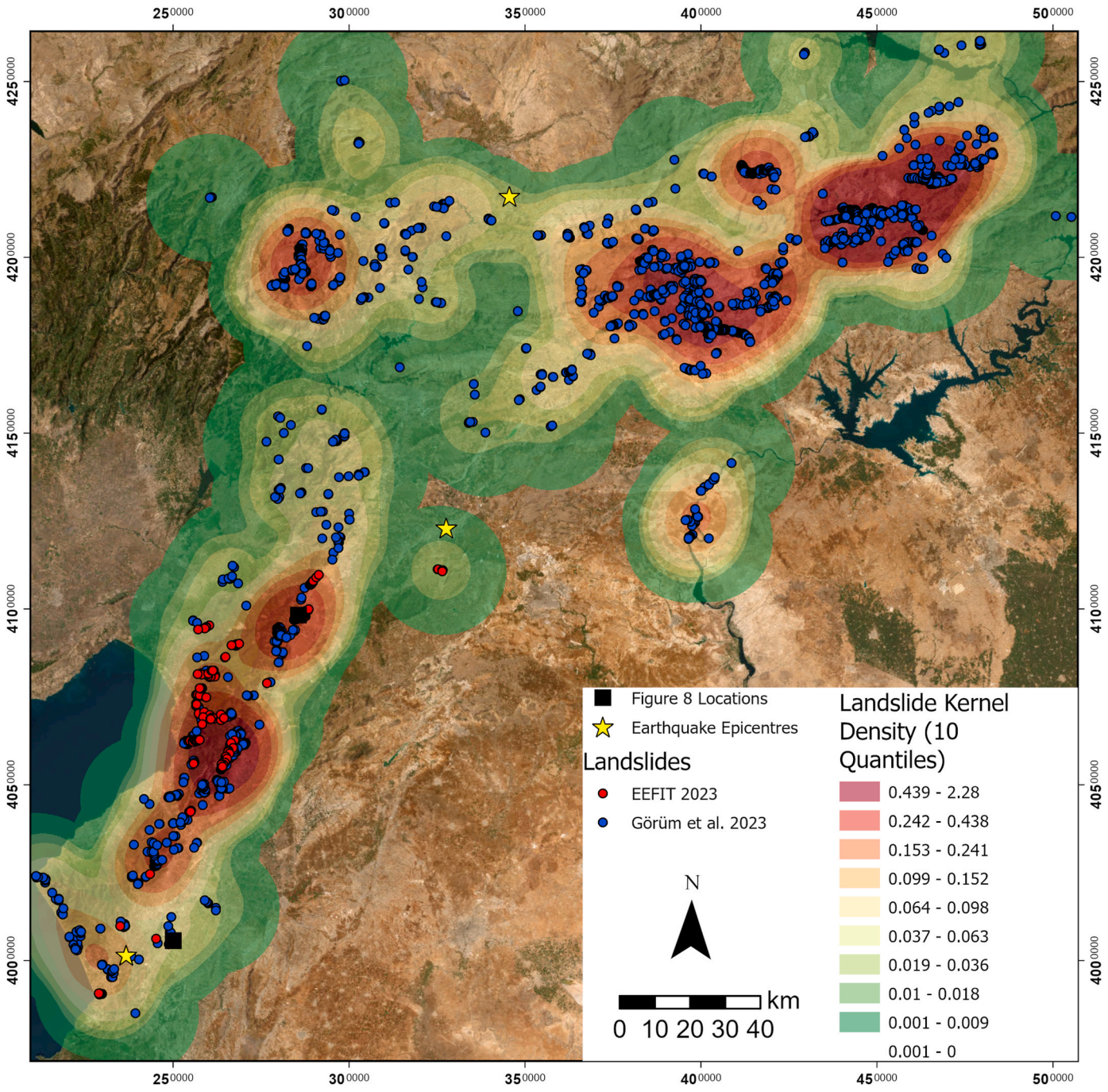

Fig. 11. Combined EEFIT and Görüm et al. (2023) landslide inventory with Kernel Density overlay. Basemap is the ESRI World View data projected in ED50 UTM Zone 37N.

critical tsunami advice to the public. KOERI, the Turkish tsunami service provider (TSP) for the NEAMTWS, issued a land threat within 15 min of the initial Pazarcık earthquake as tsunami amplitudes of up to 0.5 m were estimated along the southern coast of Türkiye (Cetin et al., 2023a). Additionally, the Italian TSP for the NEAMTWS, the Centro Allerta Tsunami (CAT) of Istituto Nazionale di Geofisica e Vulcanologia (INGV) issued a basin-watch tsunami warning for both the south and east coasts of Italy just 8 min after the mainshock (CAT-INGV, 2023). A basin-watch (red-level) tsunami warning indicates the potential for a tsunami of >0.5 m in deep ocean or a run-up of >1 m, therefore posing the risk of inundation to coastal communities that are topographically ≤ 1 m above sea level. In other regions of Türkiye and Greece, an orange-level advisory warning was issued, and other countries, including Cyprus, Albania, Montenegro, Croatia and Malta were placed on tsunami watch. Although the tsunami warnings from both TSPs were later reduced or removed, as the threat was analysed in real-time, the rapid warning responses from KOERI and INGV demonstrate the effectiveness of the tsunami early warning system that was established in 2012 (Necmioğlu et al., 2021).

Subsequent analysis of tidal gauges in the Mediterranean basin was complicated by the presence of a strong low-pressure system within the region causing a storm surge at the time of the earthquakes (Medvedeva et al., 2023). However, within 30 min of the initial M_W 7.8 Pazarcık earthquake, small amplitude tsunami waves were recorded at eight tide gauges in the Eastern Mediterranean (Cetin et al., 2023b; Medvedeva et al., 2023). The highest tsunami amplitudes were measured at

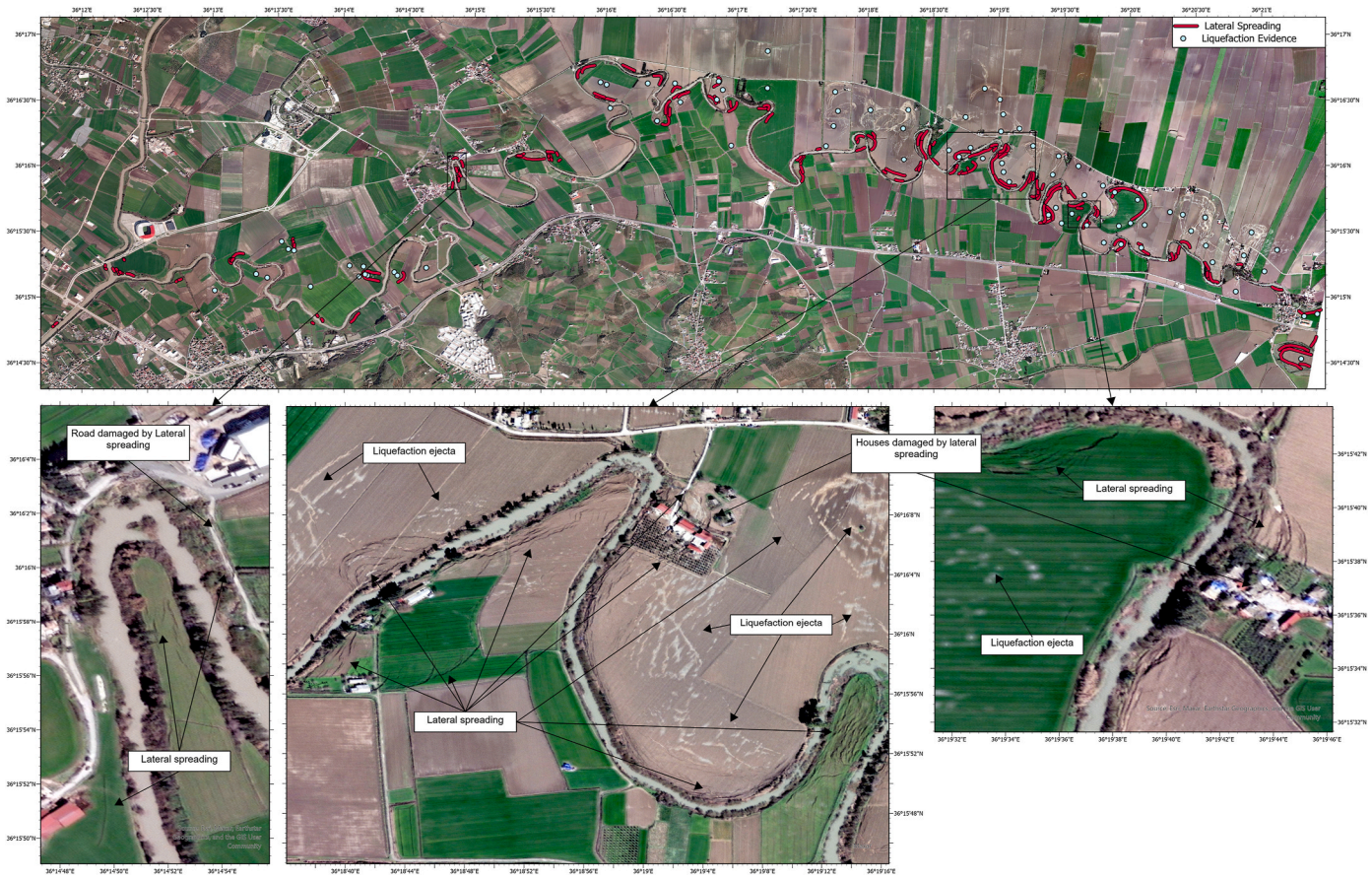

Fig. 12. Example liquefaction and lateral spreading damage mapped by EEFIT along the Orontes/Asi River.

Fumagusta station (eastern coast of Cyprus) and at Erdemli station (SE Türkiye) where wave heights of 17 cm were recorded (Cetin et al., 2023b). Additionally, 13–15 cm high waves were measured along the north coast of Cyprus (Girne station) and the south-east coast of Türkiye at the Arsuz and Bozyazı tidal gauges (Çetin et al., 2020; Medvedeva et al., 2023). While small tsunami waves of <6 cm were recorded further west along the Turkish coast at Taşucu, Antalya and Marmaris (Medvedeva et al., 2023). No waves associated with the second event were detected. Generation of a tsunami is unusual for an earthquake of this type, i.e., strike-slip and inland; modelling of the event suggests that the wave could have been generated by a submarine landslide (Heidarzadeh et al., 2023).

5.2.4. *Hydrological anomalies*

Several hydrological anomalies have been recorded in association with the Kahramanmaraş earthquakes. İnan et al. (2024) analysed groundwater samples (commercial bottled water) from two springs ~ 100 km from the epicentre of the Pazarcık earthquake, close to Osmaniye, to identify if there were any hydro-geochemical anomalies prior to the earthquakes. They showed that water from a spring emanating from a bedrock aquifer exhibited anomalies in several major ions. Increases in ions such as Ca^{2+}, Mg^{2+} and Na^{+} were seen at least 6 months prior to the earthquakes, which then reduced in the three weeks following the earthquakes. By contrast, water from a shallow alluvial aquifer showed no such geochemical changes. İnan et al. (2024) attribute these differences to the source of the water, with metamorphic bedrocks experiencing pre-earthquake stress unlike the alluvial deposits.

By contrast, Şimşek et al. (2024) collected 47 water samples from springs, wells, water treatment works and tap water following the earthquakes. They demonstrated that a number of springs experienced significant changes of flow rates and increased turbidity after the earthquakes, with high turbidity especially in samples from springs emanating from clayey limestone karstic systems with complex lithologies. One karstic spring near the town of Bahçe was recorded as ceasing to flow for a period of around 3–5 h Şimşek et al. (2024) also report ingression of saline water in coastal regions, collapse of alluvial aquifers and microbial contamination of drinking water. While the natural perturbation of many ground water systems were found to be short lived, unfortunately contamination of drinking water was more persistent with implications for human health (Şimşek et al. (2024)).

5.2.5. *Vegetation and other reports*

The final secondary effect included in the ESI 2007 scale are effects on vegetation, which are normally transient features that can be difficult to determine during field survey as the timing of vegetation damage can be unclear. Although some events such as the 2016 Mw 6.1 Peterman earthquake in Australia (King et al., 2018) can result in significant damage to shrubs and trees, during the EEFIT field survey the team observed only a single example of where a tree has undergone direct damage as a result of the fault rupture (Fig. 14). It is unclear how long such features would remain visible and will likely depend on whether the tree survives this damage or not.

6. Discussion

6.1. *ESI 2007 assessment*

The earthquake-induced environmental effects documented for the doublet Kahramanmaraş earthquakes allow the ESI 2007 intensity scale to be applied and macro-seismic intensities estimated using both primary and secondary effects. However, owing to the close association in time and space of the two main shock events it is difficult to attribute the

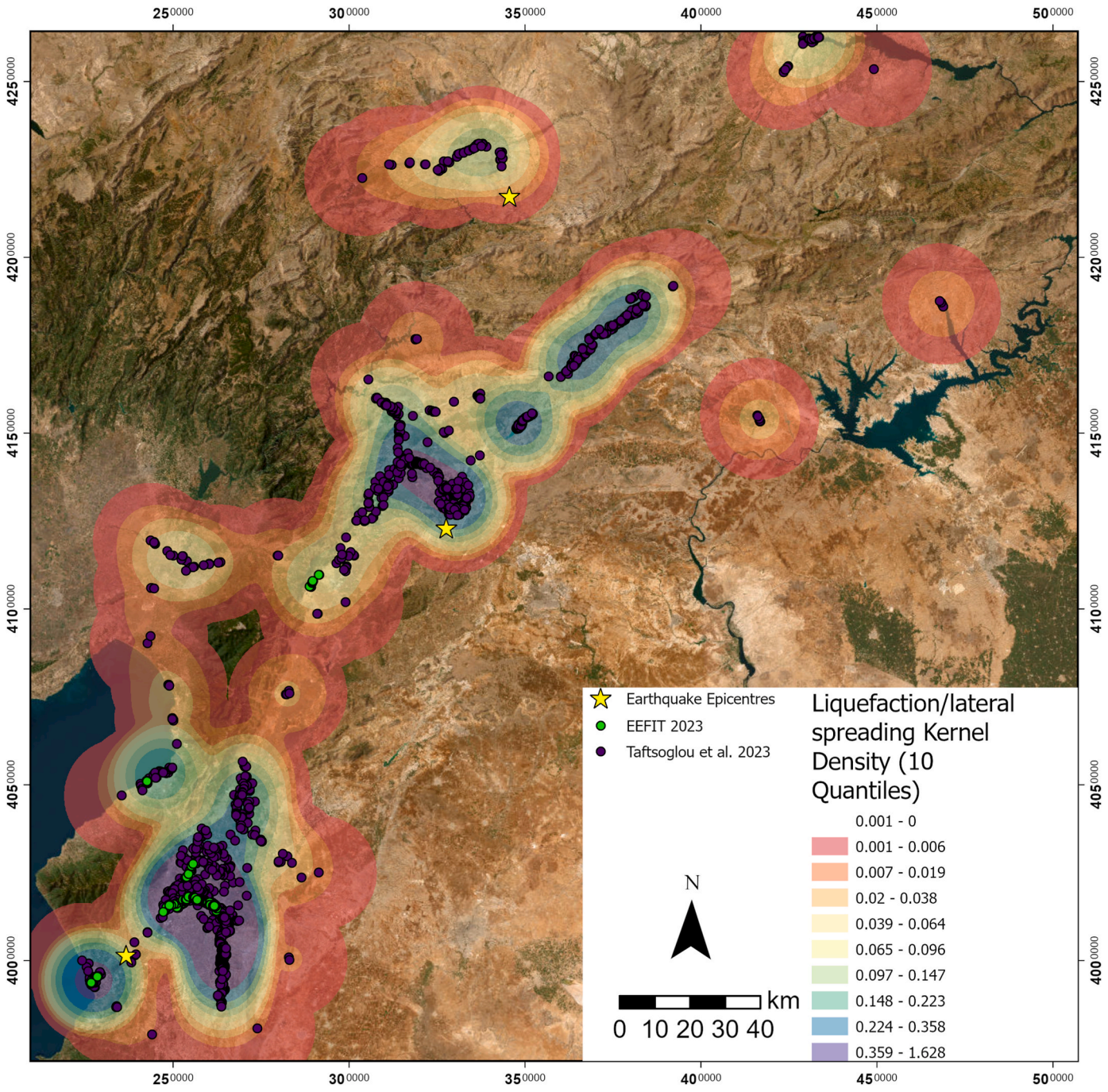

Fig. 13. Combined EEFIT and Taftsoglou et al. (2023) inventory with Kernel Density overlay. Basemap is the ESRI World View data projected in ED50 UTM Zone 37N.

wider off-fault secondary features to either event, especially where the faults converge in the north. This means that the ESI 2007 applied at site level may reflect either (or both) the Mw 7.8 Pazarcık or the Mw 7.5 Elbistan event. Similarly using the total areal extent of secondary features to determine the epicentral intensity (I_0) will represent a combined intensity.

However, the length of the surface ruptures can be reliably used to determine the epicentral intensity, I_0, for each of the main earthquake events using the parameters defined by Michetti et al. (2007) and the scaling relationships (eq. (1)) of Michetti et al. (2004):

$$I_0 = 0.4636 * \ln(x) + 8.3434 \quad \text{(Eq.1)}$$

Where x is the surface rupture length.

Therefore, the 350–375 km long fault rupture with up to 8 m of lateral displacement on the Pazarcık earthquake corresponds to a I_0 = XI; whereas the shorter Elbistan earthquake rupture of 150 km with up to 6 m of lateral displacement is consistent with an I_0 = X. These intensity values are also consistent with area effected by secondary effects, which is in the order of 35,000 km^2, and the qualitative descriptions of the intensity scale.

At site level, ESI 2007 values of XI are assigned to locations with measured displacements of >4 m (i.e., several metres); while locations with <4 m of lateral displacement ('a few metres') are assigned values of X (Fig. 15). Additionally, site specific intensities can be assigned to locations effected by landslide, liquefaction or ground water changes, albeit acknowledging that this will be a combined intensity.

Fig. 14. Field photograph showing the fault rupture causing damage to the base of a tree located on the fault (location: 37 49 13.692 N; 37 41 7.2852 E; near Gölbası).

As the co-sesimic landslide inventory consists of point, and not polygon data; the total landslide area, landslide area percentage and distribution of landslide sizes away from the rupture zone cannot be assessed. Instead the landslide number density (LND, the number of landslides per 1 km^2; c.f. Xu et al. (2013)) is calculated using a kernel density with a radius of 564.2 m equating to an area of 1 km^2. ESI 2007 intensity is subsequently defined on the LND where LND <1 is an intensity of VIII or less, 1–10 is an intensity of IX, 10–30 is an intensity of X and >30 is an intensity of XI (Xu et al., 2013). For the 3862 landslides included in the co-seismic inventory 58.3 % have a LND of ≤ 10 corresponding to a site intensity of VIII or lower, 30.2 % of events fall within a LND of 10–30 with an interpreted intensity of X, while 11.5 % have a LND of ≥ 30 representing the higher intensity of XI (Fig. 15). The highest calculated LND is 77.5 which occurs in the north of the affected area associated with the Pütürge segment of the EAFZ.

Finally, the other observed environmental effects such as temporary changes to springs, vegetation and the range of liquefaction effects are assigned ESI 2007 values of IX (Fig. 15) based upon the qualitative descriptions of intensity (Michetti et al., 2007). Whereas, the far field recorded tsunami waves can be assigned a value of IV to V. This ESI 2007 analysis demonstrates that the highest intensities of X – XI are clearly correlated with the location of the active fault or are typically within 10–15 km of the trace. The location of landslide and liquefaction effects are strongly controlled by topographic and lithological site characteristics that in some cases result in slope failures at considerable distance from the causative faults. Overall, the location of earthquake environmental effects strongly follows the distribution of PGA (Fig. 3) for both earthquakes, where ESI 2007 intensities of $>$ X correspond to regions experiencing >0.2 g PGA and where there are few EEEs where PGA did not exceed 0.05 g.

Finally, to assess the validity of the ESI 2007 assessment and to compare the Kahramanmaras earthquakes to previous events, the scaling relationships between magnitude and ESI 2007 epicentral intensity (Fig. 16) can be compared to the compilation of other strike-slip events (Ferrario et al., 2022). Although it should be noted that these are the highest magnitude strike-slip events in the catalogue. The Pazarcık earthquake falls on the regression line determined by Ferrario et al. (2022), while the Elbistan earthquake is slightly lower. This good fit to previous events demonstrates that the ESI 2007 assessment is robust although there are uncertainties associated with the landslide volumes, this is unlikely to significantly change the level or pattern of ESI.

6.1.1. *Comparison of ESI 2007 scale to other intensity scales*

One of the main advantages of using the ESI 2007 scale compared to other intensity scales is that traditional intensity scales based upon primarily built environment effects saturate at high intensities, and for the highest degrees of intensity (XI and XII) only environmental effects permit the discrimination in this upper part of the range. This effect can clearly be seen for the Kahramanmaraş earthquakes, where for the Pazarcık event the maximum intensity of IX (Modified Mercalli Intensity; MMI) is assigned by the USGS (2023) to the area adjacent to the rupture along the Amanos Fault (Supplemental Fig. 2), while 'Did you feel it' (DYFI) reports also include reports of IX intensities north along the Pazarcık and Pütürge segments of the EAFZ. Similarly, the maximum MMI intensity attributed to the Elbistan earthquake by the USGS analysis is VIII, with DFYI reports reaching MMI = IX.

Therefore, the ESI 2007 intensity estimates in the co-seismic region are higher by 1–3° than the MMI scale, which is consistent with other studies that compare ESI 2007 to instrumental intensity estimate (e.g., Naik et al., 2024). Although, DYFI reports are generally higher than the USGS MMI, these reports still fall 1–2° below the ESI 2007 determined intensity and reports are mainly located in urban areas. Indeed previous research has indicated that DYFI reports are additionally biased by socio-economic factors, as well as being more likely reported at high felt intensities (Hough, 2021; Hough and Martin, 2021).

However, the spatial correlation between MMI and ESI 2007 for the Pazarcık earthquakes shows similarities with the maximum MMI focussed along the western margin of the Amanos Rift and in the region of Kahramanmaras, following the pattern of PGA (Fig. 3A), which echoes the areas of maximum offset and thus highest site ESI 2007. Similarly, the highest MMI for the Elbistan earthquake is in the central of the Çardak Fault corresponding to the area of maximum displacement. Although, the overall MMI distribution is symmetrical with a slightly NW-SW orientation that is not consistent with the orientation of the fault or the distribution of PGA (Fig. 3B). Furthermore, the ESI 2007 assessment also indicates regions of high intensity along the northern part of the rupture, which is not reflected in the USGS MMI map but can be explained as it is an area that experienced strong PGA in both earthquakes.

6.2. *Implications*

The 2023 Pazarcık and Elbistan earthquakes appear to have no clear parallels in the historical record. The ESI 2007 intensities of XI and X, respectively, exceed even the estimated MSK intensity VIII for the 1893 earthquake (~ Mw 7.2 (Carena et al., 2023)), which has the highest estimated intensity of the pre-instrumental period. However, it is likely that only one segment of the EAFZ or DSFZ ruptured in the 19th century earthquakes based upon historical descriptions of the events. Whereas, a significant challenge of the Kahramanmaraş earthquakes assessment is the complex, multi-fault rupture, and the temporal closeness of the two main shocks combined with the occurrence of strong aftershocks not long after. These events result in a wide area of secondary environmental effects that represent the cumulative effects of the two main shocks, especially in the area where the PGA significantly overlaps. But

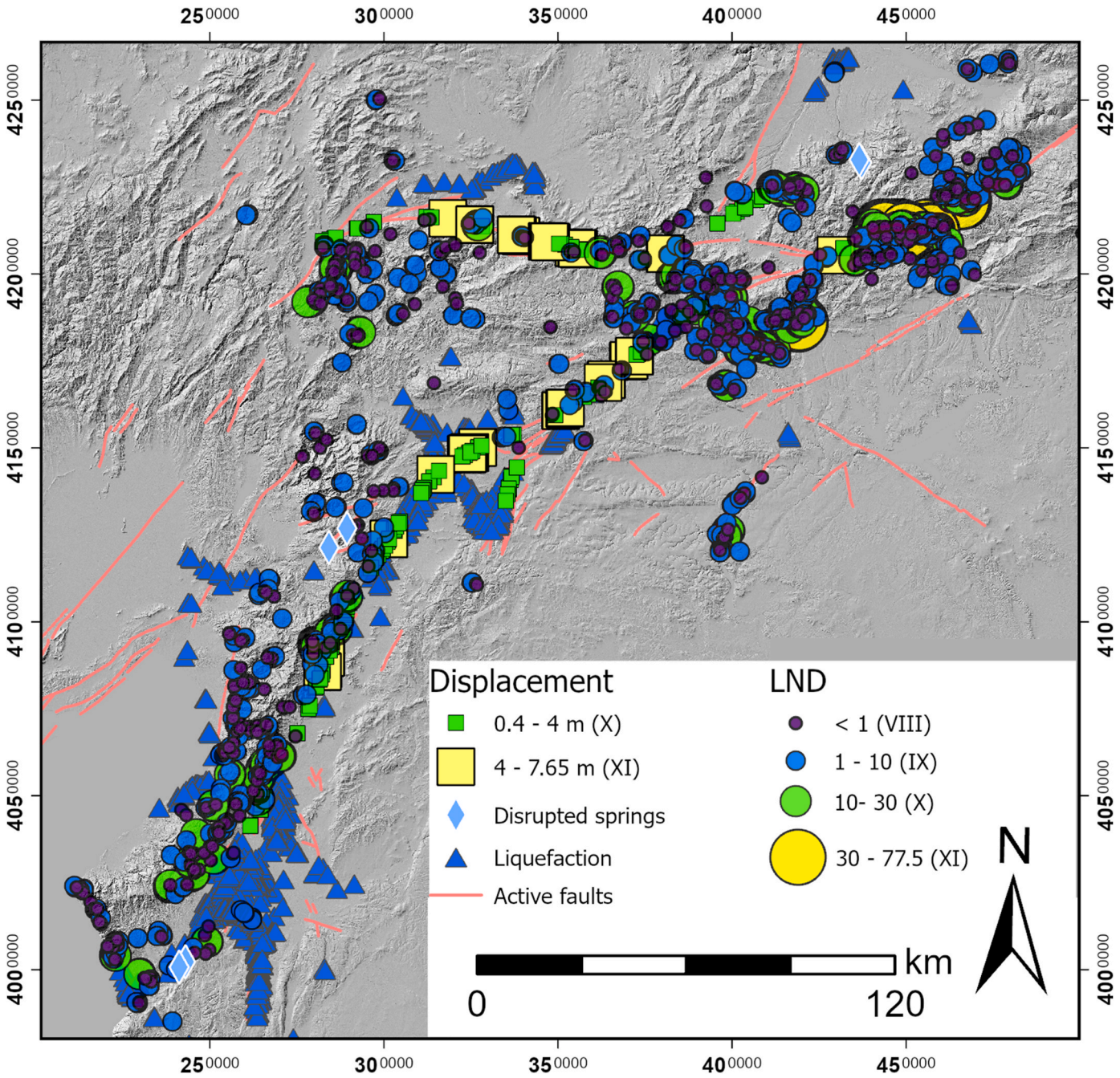

Fig. 15. Summary figure showing all recorded EEEs from the EEFIT mission and published literature with inferred ESI 2007 Intensity indicated by colour; yellow = XI; green = X; blue = IX and purple = VIII. LND = Landslide Number Density. (For interpretation of the references to colour in this figure legend, the reader is referred to the Web version of this article.)

cumulative effects cannot be ruled out over the wider region either. Similar issues have been raised for other recent complex events such as the 2016 Kaikoura earthquake and pose issues for the interpretation of EEE data both for recent and historical earthquakes (c.f., Grützner et al., 2019).

This raises the question of why the magnitude and intensity of this event is significantly greater than preceding ones. Is it because these earthquakes are unprecedented? The result of 'supercycles' as suggested by Carena et al. (2023)? Or is it that the historical records are not detailed or accurate enough?

With bias towards urban areas in modern DYFI reporting (Hough, 2021; Hough and Martin, 2021), it is not unreasonable to assume that the same issue effects historical reports leading to an underrepresentation of EEE's in remote and sparsely populated areas. Furthermore, given the level of disagreement between some catalogues on the date, location and size of events in earlier written accounts it is possible that natural complexity and large doublet type earthquakes could be mistaken for errors in historical documents. As case in point is the 1114 CE earthquake (Fig. 2a), that as Carena et al. (2023) highlights has resulted in significant disagreement in the literature about number of foreshocks, main shocks and aftershocks, and timing of this earthquake.

Therefore, the geological record is required to fill in the missing information and verify the records. However, there are few published palaeoseismic studies on the EAFZ. Yönlü and Karabacak (2024) identified only two events on the Pazarcık segment based on two trench sites.

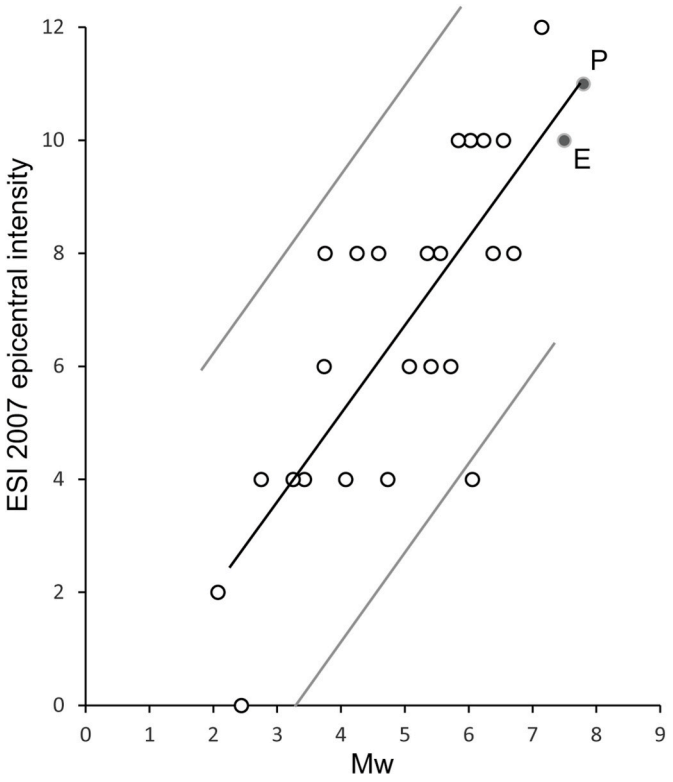

Fig. 16. Scatterplot showing linear relationship between moment magnitude and ESI 2007 I_0 for recent strike-slip earthquakes (open circles; compiled by Ferrario et al. (2022)) and the Pazarcık (P) and Elbistan (E) earthquakes, adapted from Ferrario et al. (2022).

This includes the 1114 CE earthquake potentially suggesting this event may have been comparable to the 2023 earthquakes. Although, limitations of dating techniques means that the short time (hours) between the events such as the doublet that occurred in February 2023 would not be resolvable from palaoeseismic dating. In addition, trenching studies can only define potential earthquake intensity along the fault. Yet, without such data, assessing the recurrence interval and behaviour of the fault system is not possible and the questions posed above cannot be satisfactorily answered.

Finally, the continuous rupture of the EAFZ and Amanos Fault has implications for the understanding of the geodynamics of the region. The linkage of the structures allowing rupturing across fault segments firstly suggests that previous models separating structures in the vicinity of Türkoğlu (Şengör and Yilmaz, 1981; Perinçek and Çemen, 1990; Yürür and Chorowicz, 1998; Yönlü et al., 2017) are potentially less feasible than models proposing the continuation of the EAFZ along the Amanos Fault, meeting the DSFZ at the southern end in the Amik Plain (Arpat and Saroglu, 1972; Şengör et al., 1985; Duman and Emre, 2013). Secondly, along with other recent strong earthquakes (i.e., Kaikoura, New Zealand), the complex rupture has implications for fault behaviour and segmentation in plate boundary zones.

7. Conclusions

Following the February 6 earthquake couplet, the EEFIT Hybrid mission sought to map and characterise a range of natural and built environmental effects caused by the event. These primary (fault rupture, uplift-subsidence) and secondary environmental effects (landslides, tsunamis, liquefaction etc) as reported by EEFIT are synthesised here with similar data from other field and remote-sensed studies of the event, thus allowing the robust determination of the Environmental Seismic Intensity 2007 scale. This data compilation demonstrates the significant nature of the earthquakes determining the maximum epicentral and site intensity as XI. These values are higher than estimates from other methods, consistent with other recent evaluations of ESI, demonstrating the effectiveness of this method for strong earthquakes. Additionally, comparisons to other recent and historical events suggest that this complex, multi-fault rupture does not have clear precedent, although potentially the 1114 CE earthquake could be comparable, and calls into question existing geodynamic models for the region. Consequently, it is clear that further research is required on the EAFZ/DSFZ system to fully understand the regional seismic hazard. This event, and other recent multi-fault ruptures, also serve as a tragic warning to other regions with long, complex structures but with short instrumental records or a history of only relatively small earthquakes.

CRediT authorship contribution statement

Sarah J. Boulton: Writing – original draft, Visualization, Investigation, Formal analysis, Data curation, Conceptualization. **Joshua N. Jones:** Writing – original draft, Visualization, Investigation, Formal analysis. **Fatma S. Malcioglu:** Writing – original draft, Investigation, Formal analysis. **Aisling O'Kane:** Writing – review & editing, Investigation. **Matthew D. Cleave:** Writing – review & editing, Visualization. **Orestis Adamidis:** Writing – review & editing, Investigation. **Teoman Efeoglu:** Investigation. **Yasemin Didem Aktaş:** Writing – review & editing, Resources, Project administration, Funding acquisition.

Data availability

The shapefiles for the revised fault rupture, mapped offsets, landslide and liquefaction locations mapped as part of the EEFIT mission area (described in section 5) available as follows:

Boulton (2009). EEFIT Surface Rupture Data. DOI: 10.24382/be9ed96d-787d-4bef-abc9-ab04a19d137e.

Jones et al. (2020). EEFIT Landslide Inventory, DOI: 10.24382/70498d82-6895-4ab9-bc74-d4f707cda227.

Jones et al. (2021). EEFIT Liquefaction Inventory. DOI:10.24382/825fcbbb-4ad9-4db6-848c-5ab60b81643a.

All other data referred to in this paper are available from open access data repositories or published manuscripts as cited. Digital elevation model AW3D30m data is supplied by JAXA https://www.eorc.jaxa.jp/ALOS/en/dataset/aw3d30/aw3d30_e.htm.

Declaration of competing interest

The authors declare that they have no known competing financial interests or personal relationships that could have appeared to influence the work reported in this paper.

Acknowledgements

We are grateful to the EPSRC-funded "Learning from Earthquakes: Building Resilient Communities Through Earthquake Reconnaissance, Response and Recovery" project (EP/P025641/1 and EP/P025951/1) for supporting the hybrid EEFIT mission to the February 2023 Kahramanmaraş earthquake sequence. We also acknowledge the inputs of the wider mission team that made this research possible especially Emily So, Özcan Gözenoğlu and Matthew Free. Finally, we thank the editor and reviewers (Klaus Reicherter and an anonymous reviewer) for their positive comments on the manuscript.

Appendix A. Supplementary data

Supplementary data to this article can be found online at https://doi.org/10.1016/j.quaint.2025.109804.

References

Adamidis, O., Efeoglu, T., Gozenoglu, O., Jones, J.N., Madabhushi, G.S.P., Aktas, Y.D., So, E., 2023. Geotechnical observations from the Kahramanmaraş EEFIT mission. Ground Eng. 25–28.

AFAD-DDB: Afet ve Acil Durum Yönetimi Başkanlığı, Deprem Dairesi Başkanlığı; https://deprem.afad.gov.tr/.

Aktas, Y.D., Ioannou, I., Malcioglu, F.S., Kontoe, M., Parammal Vatteri, A., Baiguera, M., Black, J., Kosker, A., Dermanis, P., Esabalioglou, M., Cabuk, E., Donmez, K., Ercolino, M., Asinari, M., Verrucci, E., Putrino, V., Durmaz, B., Kazantzidou-Firtinidou, D., Cotton, D., O'Kane, A., Ozden, A.T., Contreras, D., Cels, J., Free, M., Burton, P., Wilkinson, S., Rostami, R., D'Ayala, D., 2022. Hybrid reconnaissance mission to the 30 october 2020 aegean sea earthquake and tsunami (izmir, Turkey & samos, Greece): description of data collection methods and damage. Front. Built Environ. 8. https://doi.org/10.3389/fbuil.2022.840192.

Aktas, Y., So, E., Johnson, C., Donmez, K., Ozden, A., Parammal Vatteri, A., O'Kane, A., Kalkan, A., Andonov, A., Verrucci, E., others, 2024. The Türkiye earthquake sequence of February 2023: a longitudinal study report by EEFIT. Available at: https://www.istructe.org/resources/report/eefit-mission-report-turkey-february-2023/.

Al-Tarazi, E.A., 1999. Regional seismic hazard study for the eastern mediterranean (trans-Jordan, levant and antakia) and sinai region. J. Afr. Earth Sci. 28, 743–750. https://doi.org/10.1016/S0899-5362(99)00042-1.

Allen, M.B., Armstrong, H.A., 2008. Arabia–Eurasia collision and the forcing of mid-Cenozoic global cooling. Palaeogeogr. Palaeoclimatol. Palaeoecol. 265, 52–58.

Allstadt, K.E., Thompson, E.M., Jibson, R.W., Wald, D.J., Hearne, M., Hunter, E.J., Fee, J., Schovanec, H., Slosky, D., Haynie, K.L., 2022. The US Geological Survey ground failure product: near-real-time estimates of earthquake-triggered landslides and liquefaction. Earthq. Spectra 38, 5–36. https://doi.org/10.1177/87552930211032685.

Ambraseys, N., 2009. Earthquakes in the Mediterranean and Middle East: a Multidisciplinary Study of Seismicity up to 1900. Cambridge University Press.

Arpat, E., Saroglu, F., 1972. The East Anatolian fault system: thoughts on its development. Bull. Miner. Res. Explor. Inst. Turk. 78, 33–39.

Atanasova, M., Raykova, P., Nikolov, H., 2023. Determining the deformations of the earth's surface after the earthquakes in Turkey-Syria of 06 february 2023-initial results. In: Proceedings of the Bulgarian Academy of Sciences, pp. 554–562.

Barbot, S., Luo, H., Wang, T., Hamiel, Y., Piatibratova, O., Javed, M.T., Braitenberg, C., Gurbuz, G., 2023. Slip distribution of the february 6, 2023 Mw 7.8 and Mw 7.6, Kahramanmaraş, Turkey earthquake sequence in the East Anatolian Fault Zone. Seismica 2. https://doi.org/10.26443/seismica.v2i3.502.

Ben-Avraham, Z., 1978. The structure and tectonic setting of the Levant continental margin, Eastern Mediterranean. Tectonophysics 46, 313–331.

Boulton, S.J., 2009. Record of cenozoic sedimentation from the Amanos mountains, southern Turkey: implications for the inception and evolution of the arabia-eurasia continental collision. Sediment. Geol. 216, 29–47.

Boulton, S.J., 2013. Tectonic development of the southern Karasu Valley, Turkey: successive structural events during basin formation. Geol. Soc. Lond. Spec. Publ. 372 (1), 531–546. https://doi.org/10.1144/sp372.

Boulton, S.J., Robertson, A.H.F., 2008. The Neogene–Recent Hatay Graben, South Central Turkey: graben formation in a setting of oblique extension (transtension) related to post-collisional tectonic escape. Geol. Mag. 145.

Boulton, S.J., Robertson, A.H.F., Unlugenc, U.C., 2006. Tectonic and Sedimentary Evolution of the Cenozoic Hatay Graben, Southern Turkey: a Two-phase Model for Graben Formation, vol. 260. Geological Society, London, Special Publications, pp. 613–634.

Bozkurt, E., 2001. Neotectonics of Turkey–a synthesis. Geodin. Acta 14, 3–30.

Bulut, F., Bohnhoff, M., Eken, T., Janssen, C., Kılıç, T., Dresen, G., 2012. The East Anatolian Fault Zone: seismotectonic setting and spatiotemporal characteristics of seismicity based on precise earthquake locations. J. Geophys. Res. Solid Earth 117. https://doi.org/10.1029/2011JB008966.

Carena, S., Friedrich, A.M., Verdecchia, A., Kahle, B., Rieger, S., Kübler, S., 2023. Identification of source faults of large earthquakes in the Turkey-Syria border region between 1000 CE and the present, and their relevance for the 2023 Mw 7.8 Pazarcık earthquake. Tectonics 42, e2023TC007890. https://doi.org/10.1029/2023TC007890.

Çetin, K.Ö., Ilgaç, M., Can, G., Çakır, E., Söylemez, B., 2020. Preliminary Report on Engineering and Geological Effects of the January 24, 2020 Magnitude 6.7 Earthquake in Elazığ. Turkey. GEER-065. https://doi.org/10.17603/ds2-9jz1-e287.

Cetin, K.O., Bray, J.D., Frost, J.D., Hortacsu, A., Miranda, E., Moss, R.E.S., Stewart, J., 2023a. 2023 Türkiye Earthquakes: Report on Geoscience and Engineering Impacts. Earthquake Engineering Research Institute (GEER Association Report No. 82), LFE Program.

Cetin, K.O., Ilgaç, M., Can, G., Cakir, E., 2023b. Preliminary Reconnaissance Report on February 6, 2023, Pazarcık Mw=7.7 and Elbistan Mw=7.6, Kahramanmaraş-Türkiye Earthquakes (No. METU/EERC 2023-01). MIDDLE EAST TECHNICAL UNIVERSITY. EARTHQUAKE ENGINEERING RESEARCH CENTER.

Chang, M., Kuo, C.P., Hsu, R.E., Shau, S.H., Lin, T.M., 2012. Liquefaction potential and post-liquefaction settlement evaluations of the chuoshui river alluvial fan in taiwan. Bull. Eng. Geol. Environ. 71, 325–336.

Cornish, V., 1908. The Jamaica earthquake (1907). Geogr. J. 31, 245–271.

Cubrinovski, M., Robinson, K., 2016. Lateral spreading: evidence and interpretation from the 2010–2011 Christchurch earthquakes. Soil Dynam. Earthq. Eng. 91, 187–201.

Davison, C., 1921. On scales of seismic intensity and on the Construction and use of Isoseismal Lines. Bull. Seismol. Soc. Am. 11, 95–130. https://doi.org/10.1785/BSSA0110020095.

Dewey, J.F., Şengör, A.Cel, 1979. Aegean and surrounding regions: complex multiplate and continuum tectonics in a convergent zone. Geol. Soc. Am. Bull. 90, 84–92.

Dewey, J.F., Hempton, M.R., Kidd, W.S.F., Saroglu, F., Şengör, A.M.C., 1986. Shortening of continental lithosphere: the neotectonics of Eastern Anatolia — a young collision zone. Geol. Soc. Lond. Spec. Publ. 19, 1–36. https://doi.org/10.1144/GSL.SP.1986.019.01.01.

Duman, T.Y., Emre, Ö., 2013. The East Anatolian Fault: geometry, segmentation and jog characteristics. Geol. Soc. Lond. Spec. Publ. 372, 495–529.

Emre, Ö., Duman, T.Y., Özalp, S., Şaroğlu, F., Olgun, Ş., Elmacı, H., Çan, T., 2018. Active fault database of Turkey. Bull. Earthq. Eng. 16, 3229–3275. https://doi.org/10.1007/s10518-016-0041-2.

Erol, O., Pirazzoli, P.A., 1992. Seleucia Pieria: an ancient harbour submitted to two successive uplifts. Int. J. Naut. Archaeol. 21, 317–327. https://doi.org/10.1111/j.1095-9270.1992.tb00379.x.

Ferrario, M.F., Livio, F., Michetti, A.M., 2022. Fifteen years of Environmental Seismic Intensity (ESI-07) scale: dataset compilation and insights from empirical regressions. Quat. Int. 625, 107–119. https://doi.org/10.1016/j.quaint.2022.04.011.

Goldberg, D.E., Taymaz, T., Reitman, N.G., Hatem, A.E., Yolsal-Çevikbilen, S., Barnhart, W.D., Irmak, T.S., Wald, D.J., Öcalan, T., Yeck, W.L., Özkan, B., Thompson Jobe, J.A., Shelly, D.R., Thompson, E.M., DuRoss, C.B., Earle, P.S., Briggs, R.W., Benz, H., Erman, C., Doğan, A.H., Altuntaş, C., 2023. Rapid characterization of the february 2023 Kahramanmaraş, Türkiye, earthquake sequence. Seism. Rec. 3, 156–167. https://doi.org/10.1785/0320230009.

Görüm, T., Tanyas, H., Karabacak, F., Yılmaz, A., Girgin, S., Allstadt, K.E., Süzen, M.L., Burgi, P., 2023. Preliminary documentation of coseismic ground failure triggered by the February 6, 2023 Türkiye earthquake sequence. Eng. Geol. 327, 107315. https://doi.org/10.1016/j.enggeo.2023.107315.

Grützner, C., Walker, R., Ainscoe, E., Elliott, A., Abdrakhmatov, K., 2019. Earthquake environmental effects of the 1992 MS7.3 suusamyr earthquake, Kyrgyzstan, and their implications for paleo-earthquake studies. Geosciences 9, 271. https://doi.org/10.3390/geosciences9060271.

Guidoboni, E., Comastri, A., 2005. Catalogue of Earthquakes and Tsunamis in the Mediterranean Area from the 11th to the 15th Century. Istituto Nazionale di Geofisica e Vulcanologia—Storia Geofisica Ambiente (INGV-SGA).

Guidoboni, E., Traina, G., Comastri, A., 1994. Catalogue of Ancient Earthquakes in the Mediterranean Sea up to the 10th Century. Istituto nazionale di geofisica.

Guo, Y., Li, H., Liang, P., Xiong, R., Chaozhong, H., Xu, Y., 2023. Preliminary report of coseismic surface rupture (part) of Turkey's Mw7. 8 earthquake by remote sensing interpretation. Earthq. Res. Adv., 100219

Hardenberg, M.F., Robertson, A.H., 2007. Sedimentology of the NW margin of the Arabian plate and the SW–NE trending Nahr El-Kabir half-graben in northern Syria during the latest Cretaceous and Cenozoic. Sediment. Geol. 201, 231–266.

He, L., Feng, G., Xu, W., Wang, Y., Xiong, Z., Gao, H., Liu, X., 2023. Coseismic kinematics of the 2023 Kahramanmaras, Turkey earthquake sequence from InSAR and optical data. Geophys. Res. Lett. 50, e2023GL104693. https://doi.org/10.1029/2023GL104693.

Heidarzadeh, M., Gusman, A.R., Mulia, I.E., 2023. The landslide source of the eastern Mediterranean tsunami on 6 February 2023 following the Mw 7.8 Kahramanmaraş (Türkiye) inland earthquake. Geosci. Lett. 10, 50. https://doi.org/10.1186/s40562-023-00304-8.

Hough, S.E., 2021. Contributed reports of widely felt earthquakes in California, United States: if they felt it, did they report it? Front. Earth Sci. 9. https://doi.org/10.3389/feart.2021.770445.

Hough, S.E., Martin, S.S., 2021. Which earthquake accounts matter? Seismol Res. Lett. 92, 1069–1084. https://doi.org/10.1785/0220200366.

İnan, S., Çetin, H., Yakupoğlu, N., 2024. Spring water anomalies before two consecutive earthquakes (M_w 7.7 and M_w 7.6) in Kahramanmaraş (Türkiye) on 6 February 2023. Nat. Hazards Earth Syst. Sci. 24, 397–409. https://doi.org/10.5194/nhess-24-397-2024.

Jia, Z., Jin, Z., Marchandon, M., Ulrich, T., Gabriel, A.-A., Fan, W., Shearer, P., Zou, X., Rekoske, J., Bulut, F., Garagon, A., Fialko, Y., 2023. The complex dynamics of the 2023 Kahramanmaraş, Turkey, Mw 7.8-7.7 earthquake doublet. Science 381, 985–990. https://doi.org/10.1126/science.adi0685.

Jones, J.N., Stokes, M., Boulton, S.J., Bennett, G.L., Whitworth, M.R.Z., 2020. Coseismic and monsoon-triggered landslide impacts on remote trekking infrastructure, Langtang Valley. Nepal. Q. J. Eng. Geol. Hydrogeol. 53, 159–166. https://doi.org/10.1144/qjegh2019-048.

Jones, J.N., Boulton, S.J., Stokes, M., Bennett, G.L., Whitworth, M.R.Z., 2021. 30-year record of Himalaya mass-wasting reveals landscape perturbations by extreme events. Nat. Commun. 12, 1–15. https://doi.org/10.1038/s41467-021-26964-8.

Karabacak, V., Altunel, E., Meghraoui, M., Akyüz, H.S., 2010. Field evidences from northern Dead Sea Fault Zone (South Turkey): new findings for the initiation age and slip rate. Tectonophysics 480, 172–182.

Karabacak, V., Özkaymak, Ç., Sözbilir, H., Tatar, O., Aktuğ, B., Özdağ, Ö.C., Çakir, R., Aksoy, E., Koçbulut, F., Softa, M., 2023. The 2023 Pazarcık (Kahramanmaraş, Türkiye) earthquake (Mw 7.7): implications for surface rupture dynamics along the East Anatolian Fault Zone. J. Geol. 180. https://doi.org/10.1144/jgs2023-020 jgs2023-020.

Karabulut, H., Güvercin, S.E., Hollingsworth, J., Konca, A.Ö., 2023. Long silence on the East Anatolian Fault Zone (Southern Turkey) ends with devastating double earthquakes (6 February 2023) over a seismic gap: implications for the seismic potential in the Eastern Mediterranean region. J. Geol. Soc. 180. https://doi.org/10.1144/jgs2023-021 jgs2023-021.

Karasözen, E., Nissen, E., Bergman, E.A., Johnson, K.L., Walters, R.J., 2016. Normal faulting in the Simav graben of western Turkey reassessed with calibrated

earthquake relocations. J. Geophys. Res. Solid Earth 121, 4553–4574. https://doi.org/10.1002/2016JB012828.
Kargel, J.S., Leonard, G., Shugar, D.H., Haritashya, U.K., Bevington, A., Fielding, E., Fujita, K., Geertsema, M., Miles, E.S., Steiner, J., Anderson, E., 2016. Geomorphic and geologic controls of geohazards induced by Nepal's 2015 Gorkha earthquake. Science 351, aac8353. https://doi.org/10.1126/science.aac8353.
Kempler, D., Garfunkel, Z., 1994. Structures and kinematics in the northeastern Mediterranean: a study of an irregular plate boundary. Tectonophysics 234, 19–32.
King, T.R., Quigley, M.C., Clark, D., 2018. Earthquake environmental effects produced by the Mw 6.1, 20th May 2016 Petermann earthquake, Australia. Tectonophysics 747–748, 357–372. https://doi.org/10.1016/j.tecto.2018.10.010.
Kobayashi, T., Munekane, H., Kuwahara, M., Furui, H., 2024. Insights on the 2023 Kahramanmaraş Earthquake, Turkey, from InSAR: fault locations, rupture styles and induced deformation. Geophys. J. Int. 236, 1068–1088. https://doi.org/10.1093/gji/ggad464.
Kozaci, O., Altunel, E., Koehler, R., Yildirim, C., Clahan, K., 2024. M7.8 Kahramanmaras earthquake surface fault rupture and near-fault effect observations. Jpn. Geotech. Soc. Spec. Publ. 10, 276–281. https://doi.org/10.3208/jgssp.v10.SS-6-03.
Kurcer, A., Elmaci, H., Ozdemir, E., Guven, C., Guler, C., Avcu, I., Ozalp, S., 2023. 06 ŞUBAT 2023 PAZARCIK (KAHRAMANMARAŞ) DEPREMİ (Mw 7,7) SAHA GÖZLEM RAPORLARI SERİSİ 1- AMANOS SEGMENTİ (No. 14121). MADEN TETKİK VE ARAMA GENEL MÜDÜRLÜĞÜ.
Le Pichon, X., Angelier, J., 1979. The Hellenic arc and trench system: a key to the neotectonic evolution of the eastern Mediterranean area. Tectonophysics 60, 1–42.
Li, S., Wang, X., Tao, T., Zhu, Y., Qu, X., Li, Z., Huang, J., Song, S., 2023. Source model of the 2023 Turkey earthquake sequence imaged by sentinel-1 and GPS measurements: implications for heterogeneous fault behavior along the East Anatolian Fault Zone. Remote Sens. 15, 2618. https://doi.org/10.3390/rs15102618.
Li, W., Zhao, L., Tan, K., Lu, X., Zhang, C., Li, C., Han, S., 2024. Coseismic deformation and fault slip distribution of the 2023 MW7. 8 and MW7. 6 earthquakes in Türkiye. Earthq. Sci. 37, 263–276.
Lomax, A., 2023. Precise, NLL-SSST-coherence hypocenter catalog for the 2023 Mw 7.8 and Mw 7.6 SE Turkey earthquake sequence. https://doi.org/10.5281/zenodo.7699882.
Lort, J.M., 1971. The tectonics of the eastern Mediterranean: a geophysical review. Rev. Geophys. 9, 189–216. https://doi.org/10.1029/RG009i002p00189.
Lyberis, N., Yurur, T., Chorowicz, J., Kasapoglu, E., Gundogdu, N., 1992. The East Anatolian Fault: an oblique collisional belt. Tectonophysics 204, 1–15.
Mai, P.M., Aspiotis, T., Aquib, T.A., Cano, E.V., Castro-Cruz, D., Espindola-Carmona, A., Li, B., Li, X., Liu, J., Matrau, R., Nobile, A., Palgunadi, K.H., Ribot, M., Parisi, L., Suhendi, C., Tang, Y., Yalcin, B., Avşar, U., Klinger, Y., Jónsson, S., 2023. The destructive earthquake doublet of 6 february 2023 in south-central Türkiye and northwestern Syria: initial observations and analyses. Seism. Rec. 3, 105–115. https://doi.org/10.1785/0320230007.
Marc, O., Hovius, N., Meunier, P., Uchida, T., Hayashi, S., 2015. Transient changes of landslide rates after earthquakes. Geology 43, 883–886.
Martha, T.R., Babu Govindharaj, K., Vinod Kumar, K., 2015. Damage and geological assessment of the 18 September 2011 Mw 6.9 earthquake in Sikkim, India using very high resolution satellite data. Geosci. Front., Special Issue 6, 793–805. https://doi.org/10.1016/j.gsf.2013.12.011.
McKenzie, D., 1978. Active tectonics of the alpine—himalayan belt: the aegean sea and surrounding regions. Geophys. J. Int. 55, 217–254.
Medvedeva, A., Vydrin, D., Krylov, A., Shiryborova, A., Smirnova, D., Tsukanova, E., Kânoğlu, U., Medvedev, I., 2023. The Turkish tsunami of 6 february 2023 in the northeastern mediterranean. Pure Appl. Geophys. 180, 3177–3193. https://doi.org/10.1007/s00024-023-03341-8.
Meghraoui, M., Gomez, F., Sbeinati, R., Van der Woerd, J., Mouty, M., Darkal, A.N., Radwan, Y., Layyous, I., Al Najjar, H., Darawcheh, R., Hijazi, F., Al-Ghazzi, R., Barazangi, M., 2003. Evidence for 830 years of seismic quiescence from palaeoseismology, archaeoseismology and historical seismicity along the Dead Sea fault in Syria. Earth Planet Sci. Lett. 210, 35–52. https://doi.org/10.1016/S0012-821X(03)00144-4.
Melgar, D., Taymaz, T., Ganas, A., Crowell, B.W., Öcalan, T., Kahraman, M., Tsironi, V., Yolsal-Çevikbil, S., Valkaniotis, S., Irmak, T.S., 2023. Sub-and Super-shear Ruptures during the 2023 Mw 7.8 and Mw 7.6 Earthquake Doublet in SE Türkiye. Seismica 2 (3). https://doi.org/10.26443/seismica.v2i3.387.
Michetti, A., Esposito, E., Mohammadioun, B., Mohammadioun, J., Gurpinar, A., Porfido, S., Rogozhin, E., Serva, L., Tatevossian, R., Vittori, E., 2004. The INQUA Scale: an Innovative Approach for Assessing Earthquake Intensities Based on Seismically-Induced Ground Effects in the Environment. In: Special Paper, Memorie Descrittive Della Carta Geologica D'Italia, Vol. LXVII, pp. 1–116.
Michetti, A., Audemard, F., Azuma, T., Clague, J., Comerci, V., Esposito, E., Guerrieri, L., Grpinar, A., McCalpin, J., Mohammadioun, B., 2007. Environmental Seismic Intensity Scale 2007-ESI 2007. In: Memorie Descrittive Della Carta Geologica D'Italia, Vol. 74, p. 41.
Mikhailov, V.O., Babayantz, I.P., Volkova, M.S., Timoshkina, E.P., Smirnov, V.B., Tikhotskiy, S.A., 2023. The february 6, 2023, earthquakes in Turkey: a model of the rupture surface based on satellite radar interferometry. Dokl. Earth Sci. 511, 571–577. https://doi.org/10.1134/S1028334X23600627.
Mosquera-Machado, S., Lalinde-Pulido, C., Salcedo-Hurtado, E., Michetti, A.M., 2009. Ground effects of the 18 october 1992, murindo earthquake (NW Colombia), using the environmental seismic intensity scale (ESI 2007) for the assessment of intensity. In: Reicherter, K., Michetti, A.M., Silva, P.G. (Eds.), Palaeoseismology, Historical and Prehistorical Records of Earthquake Ground Effects for Seismic Hazard Assessment, vol. 316. Geol. Soc. Lond. Spec. Publ., pp. 123–144. https://doi.org/10.1144/SP316.7
Moss, R.E., Altunel, E., Bassal, P., Bray, J.D., Buckreis, T.E., Cetin, K.O., Clahan, K., Duman, E., Frost, D., Hashash, Y., Koehler, R.D., Kozaci, O., Lozano, J.M., Macedo, J., Moug, D., Nichols, E., Pehlivan, M., Pretell, R., Stewart, J.P., Ulmer, K.J., Yildirim, C., 2024. Geotechnical and geological reconnaissance observations of the 6 February 2023 Türkiye earthquakes. Earthq. Spectra, 87552930241281007. https://doi.org/10.1177/87552930241281007.
Naik, S.P., Mohanty, A., Mittal, H., Porfido, S., Michetti, A.M., Yang, B.M., Gwon, O., Kim, Y.-S., 2023. The earthquake environmental effects (EEEs) of the 6th February 2018, Hualien earthquake (Mw=6.4): a contribution to the seismic hazard estimation in the epicentral area. Quat. Int. 656, 48–69. https://doi.org/10.1016/j.quaint.2022.10.009.
Naik, S.P., Rimando, J.M., Mittal, H., Rimando, R.E., Porfido, S., Kim, Y.-S., 2024. Reappraisal of the 2012 magnitude (MW) 6.7 Negros Oriental (Philippines) earthquake intensity and ShakeMap generation by using ESI-2007 environmental effects. Geomat. Nat. Hazards Risk 15, 2311890. https://doi.org/10.1080/19475705.2024.2311890.
Necmioğlu, Ö., Turhan, F., Özer Sözdinler, C., Yılmazer, M., Güneş, Y., Cambaz, M.D., Altuncu Poyraz, S., Ergün, T., Kalafat, D., Özener, H., 2021. KOERI's tsunami warning system in the eastern mediterranean and its connected seas: a decade of achievements and challenges. Appl. Sci. 11, 11247.
Nofl, D., Darwishe, H., Chaaban, F., Mohammad, A., 2023. Mapping surface displacements after the 6 February 2023 earthquake in Syria and Turkey using DInSAR and GIS techniques. Spat. Inf. Res. https://doi.org/10.1007/s41324-023-00552-y.
Okuwaki, R., Yagi, Y., Taymaz, T., Hicks, S.P., 2023. Multi-scale rupture growth with alternating directions in a complex fault network during the 2023 south-eastern Türkiye and Syria earthquake doublet. Geophys. Res. Lett. 50, e2023GL103480. https://doi.org/10.1029/2023GL103480.
Ota, Y., Azuma, T., Lin, Y.N., 2009. Application of INQUA environmental seismic intensity scale to recent earthquakes in Japan and taiwan. In: Reicherter, K., Michetti, A.M., Silva, P.G. (Eds.), Palaeoseismology, Historical and Prehistorical Records of Earthquake Ground Effects for Seismic Hazard Assessment, vol. 316. Geol. Soc. Lond. Spec. Publ., pp. 55–71. https://doi.org/10.1144/SP316.4
Ou, Q., Lazecky, M., Watson, C.S., Maghsoudi, Y., Wright, T., 2023. 3D displacements and strain from the 2023 february Turkey earthquakes, version 1. https://doi.org/10.5285/DF93E92A3ADC46B9A5C4BD3A547CD242.
Papanikolaou, I., Melaki, M., 2017. The Environmental Seismic Intensity Scale (ESI 2007) in Greece, addition of new events and its relationship with magnitude in Greece and the Mediterranean; preliminary attenuation relationships. Quat. Int. 451, 37–55. https://doi.org/10.1016/j.quaint.2017.05.044.
Papanikolaou, I.D., Van Balen, R., Silva, P.G., Reicherter, K., 2015. Geomorphology of active faulting and seismic hazard assessment: new tools and future challenges. Geomorphol. Geomorphol. Active Faulting Seismic Hazard Assess.: New Tools Future Challen. 237, 1–13. https://doi.org/10.1016/j.geomorph.2015.02.024.
Papathanassiou, G., Valkaniotis, S., Ganas, A., Stampolidis, A., Rapti, D., Caputo, R., 2022. Floodplain evolution and its influence on liquefaction clustering: the case study of March 2021 Thessaly, Greece, seismic sequence. Eng. Geol. 298, 106542. https://doi.org/10.1016/j.enggeo.2022.106542.
Parker, R.N., Hancox, G.T., Petley, D.N., Massey, C.I., Densmore, A.L., Rosser, N.J., 2015. Spatial distributions of earthquake-induced landslides and hillslope preconditioning in the northwest South Island, New Zealand. Earth Surf. Dyn. 3, 501–525. https://doi.org/10.5194/esurf-3-501-2015.
Perinçek, D., Çemen, I., 1990. The structural relationship between the East Anatolian and Dead Sea fault zones in southeastern Turkey. Tectonophysics 172, 331–340.
Petersen, G.M., Büyükakpinar, P., Vera Sanhueza, F.O., Metz, M., Cesca, S., Akbayram, K., Saul, J., Dahm, T., 2023. The 2023 southeast Türkiye seismic sequence: rupture of a complex fault network. Seism. Rec. 3, 134–143. https://doi.org/10.1785/0320230008.
Pousse-Beltran, L., Nissen, E., Bergman, E.A., Cambaz, M.D., Gaudreau, É., Karasözen, E., Tan, F., 2020. The 2020 6.8 elazığ (Turkey) earthquake reveals rupture behavior of the East Anatolian Fault. Geophys. Res. Lett. 47, e2020GL088136. https://doi.org/10.1029/2020GL088136.
Reicherter, K., Michetti, A.M., Silva, P.G., 2009. Palaeoseismology: historical and prehistorical records of earthquake ground effects for seismic hazard assessment. In: Reicherter, K., Michetti, A.M., Silva, P.G. (Eds.), Palaeoseismology, Historical and Prehistorical Records of Earthquake Ground Effects for Seismic Hazard Assessment, vol. 316. Geol. Soc. Lond. Spec. Publ., pp. 1–10. https://doi.org/10.1144/SP316.1
Reilinger, R., McClusky, S., Vernant, P., Lawrence, S., Ergintav, S., Cakmak, R., Ozener, H., Kadirov, F., Guliev, I., Stepanyan, R., 2006. GPS constraints on continental deformation in the Africa-Arabia-Eurasia continental collision zone and implications for the dynamics of plate interactions. J. Geophys. Res. Solid Earth 111.
Reitman, N.G., Briggs, Richard, Barnhart, William D., Jobe, Jessica A., Duross, Christopher B., Hatem, Alexandra E., Gold, Ryan D., Akçiz, Sinan, Koehler, Richard, Mejstrik, John D., Collett, Camille M., 2024. Fault rupture mapping of the 6 february 2023 Kahramanmaraş, Türkiye, earthquake sequence from satellite data (ver. 1.1, february 2024). https://doi.org/10.5066/P985I7U2.
Robertson, A.H., 1998. Mesozoic-Tertiary tectonic evolution of the easternmost Mediterranean area: integration of marine and land evidence. Proc. Ocean Drill. Progr. Sci. Results 160. Chapter 54.
Provost, F., Karabacak, V., Malet, J.-P., Van der Woerd, J., Meghraoui, M., Masson, F., Ferry, M., MMichéa, D., Pointal, E., 2024. High-resolution co-seismic fault offsets of the 2023 Türkiye earthquake ruptures using satellite imagery. Sci. Rep. 14, 6834. https://doi.org/10.1038/s41598-024-55009-5.
Robertson, A.H.F., Parlak, O., 2024. Eocene contractional deformation in the NW corner of the Arabian plate and its relation to Arabia-Eurasia collision in SE Türkiye. Int. Geol. Rev. 0, 1–37. https://doi.org/10.1080/00206814.2024.2400696.

Saroglu, F., 1992. The East Anatolian Fault Zone of Turkey. Ann Tectonicae, pp. 99–125.
Şengör, A.C., Yilmaz, Y., 1981. Tethyan evolution of Turkey: a plate tectonic approach. Tectonophysics 75, 181–241.
Şengör, A.M.C., Görür, N., Şaroğlu, F., 1985. Strike-slip faulting and related basin formation in zones of tectonic escape: Turkey as a case study. In: Biddle, K.T., Christie-Blick, N. (Eds.), Strike-Slip Deformation, Basin Formation, and Sedimentation, Society of Economic Paleontologists and Mineralogists, 37, pp. 227–264. https://doi.org/10.2110/pec.85.37.
Şengör, A.C., Özeren, M.S., Keskin, M., Sakınç, M., Özbakır, A.D., Kayan, I., 2008. Eastern Turkish high plateau as a small Turkic-type orogen: implications for post-collisional crust-forming processes in Turkic-type orogens. Earth Sci. Rev. 90, 1–48.
Serva, L., 1994. Ground effects in intensity scales. Terra Nova 6, 414–416. https://doi.org/10.1111/j.1365-3121.1994.tb00515.x.
Seyrek, A., Demir, T., Pringle, M.S., Yurtmen, S., Westaway, R.W.C., Beck, A., Rowbotham, G., 2007. Kinematics of the Amanos Fault, southern Turkey, from Ar/Ar dating of offset Pleistocene basalt flows: transpression between the African and Arabian plates. In: Cunningham, W.D., Mann, P. (Eds.), Tectonics of Strike-slip Restraining and Releasing Bends, vol. 290. Geol. Soc. Lond. Spec. Publ., pp. 255–284
Silva, P.G., Guerrieri, L., Michetti, A.M., 2015. Intensity scale ESI 2007 for assessing earthquake intensities. Encycl. Earthq. Eng. 4, 1219–1237.
Şimşek, C., Akinci, G., Fistikoğlu, O., Canli, K., Sözbilir, H., Ayol, A., Bilgiç, E., 2024. Response of water resources to the Kahramanmaraş earthquakes (MW 7.7 and MW 7.6) that occurred on february 6, 2023, on the East Anatolian Fault Zone (Türkiye). Turk. J. Earth Sci. 33, 69–84. https://doi.org/10.55730/1300-0985.1899.
Softa, M., Koçbulut, F., Akgün, E., Aksoy, E., Sözbilir, H., Tatar, O., Karabacak, V., Özkaymak, Ç., Utku, M., Özdağ, Ö., Çakir, R., Demir, A., Arslan, G., 2024. Surface rupture during the 6th of February 2023 Mw 7.6 Elbistan-Ekinözü (Kahramanmaraş) earthquake: implications for fault rupture dynamics along the northern branch of East Anatolian Fault Zone. Turk. J. Earth Sci. 33, 1–21. https://doi.org/10.55730/1300-0985.1895.
Stucchi, M., Rovida, A., Gomez Capera, A.A., Alexandre, P., Camelbeeck, T., Demircioglu, M.B., Gasperini, P., Kouskouna, V., Musson, R.M.W., Radulian, M., Sesetyan, K., Vilanova, S., Baumont, D., Bungum, H., Fäh, D., Lenhardt, W., Makropoulos, K., Martinez Solares, J.M., Scotti, O., Živčić, M., Albini, P., Batllo, J., Papaioannou, C., Tatevossian, R., Locati, M., Meletti, C., Viganò, D., Giardini, D., 2013. The SHARE European earthquake catalogue (SHEEC) 1000–1899. J. Seismol. 17, 523–544. https://doi.org/10.1007/s10950-012-9335-2.
Sümer, Ö., 2024. Tepehan Rockslide: a large-scale earthquake-induced geological structure formed by Mw:7.8 Kahramanmaraş (Pazarcık) earthquake, Türkiye. Turk. J. Earth Sci. 33, 40–55. https://doi.org/10.55730/1300-0985.1897.
Taftsoglou, M., Valkaniotis, S., Papathanassiou, G., Karantanellis, E., 2023. Satellite imagery for rapid detection of liquefaction surface manifestations: the case study of Türkiye–Syria 2023 earthquakes. Remote Sens. 15, 4190. https://doi.org/10.3390/rs15174190.
Tanyaş, H., Lombardo, L., 2019. Variation in landslide-affected area under the control of ground motion and topography. Eng. Geol. 260, 105229. https://doi.org/10.1016/j.enggeo.2019.105229.
Tapponnier, P., Peltzer, G., Le Dain, A.Y., Armijo, R., Cobbold, P., 1982. Propagating extrusion tectonics in Asia: new insights from simple experiments with plasticine. Geology 10, 611–616. https://doi.org/10.1130/0091-7613(1982)10<611:PETIAN>2.0.CO;2.
Tobita, T., Kiyota, T., Torisu, S., Cinicioglu, O., Tonuk, G., Milev, N., Contreras, J., Contreras, O., Shiga, M., 2024. Geotechnical damage survey report on February 6, 2023 Turkey-Syria Earthquake, Turkey. Soils Found. 64, 101463. https://doi.org/10.1016/j.sandf.2024.101463.
Tsukamoto, Y., Ishihara, K., 2010. Analysis on settlement of soil deposits following liquefaction during earthquakes. Soils Found. 50 (3), 399–411.
USGS, 2023. M 7.8 - pazarcik earthquake, Kahramanmaras earthquake sequence [WWW Document]. URL. https://earthquake.usgs.gov/earthquakes/eventpage/us6000jllz/executive. accessed 11.25.24.
Vidal, N., Alvarez-Marrón, J., Klaeschen, D., 2000. The structure of the Africa-Anatolia plate boundary in the eastern Mediterranean. Tectonics 19, 723–739. https://doi.org/10.1029/2000TC900011.
Weinberger, R., Nuriel, P., Kylander-Clark, A.R., Craddock, J.P., 2020. Temporal and spatial relations between large-scale fault systems: evidence from the Sinai-Negev shear zone and the Dead Sea Fault. Earth Sci. Rev. 211, 103377.
Westaway, R.O.B., Arger, J.A.N., 2001. Kinematics of the Malatya–Ovacik fault zone. Geodin. Acta 14, 103–131.
Whitworth, M.R.Z., Giardina, G., Penney, C., Di Sarno, L., Adams, K., Kijewski-Correa, T., Black, J., Foroughnia, F., Macchiarulo, V., Milillo, P., Ojaghi, M., Orfeo, A., Pugliese, F., Dönmez, K., Aktas, Y.D., Macabuag, J., 2022. Lessons for remote post-earthquake reconnaissance from the 14 August 2021 Haiti earthquake. Front. Built Environ. 8. https://doi.org/10.3389/fbuil.2022.873212.
Xu, C., Xu, X., Zhou, B., Yu, G., 2013. Revisions of the M 8.0 Wenchuan earthquake seismic intensity map based on co-seismic landslide abundance. Nat. Hazards 69, 1459–1476. https://doi.org/10.1007/s11069-013-0757-0.
Yönlü, Ö., Karabacak, V., 2024. Surface rupture history and 18 kyr long slip rate along the Pazarcık segment of the East Anatolian Fault. J. Geol. Soc. 181, jgs2023–j2056. https://doi.org/10.1144/jgs2023-056.
Yönlü, Ö., Altunel, E., Karabacak, V., 2017. Geological and geomorphological evidence for the southwestern extension of the East Anatolian Fault Zone, Turkey. Earth Planet Sci. Lett. 469, 1–14.
Youd, T. Leslie, 1973. Liquefaction, Flow, and Associated Ground Failure, vol. 688. US Geological Survey.
Yürür, M.T., Chorowicz, J., 1998. Recent volcanism, tectonics and plate kinematics near the junction of the African, Arabian and Anatolian plates in the eastern Mediterranean. J. Volcanol. Geoth. Res. 85, 1–15.